Experimental Study of the HUM Control Operator for Linear Waves

Gilles Lebeau, Maëlle Nodet

Experimental Study of the HUM Control Operator for Linear Waves

Gilles Lebeau*† — Université de Nice
Maëlle Nodet‡ — Université de Grenoble, INRIA

April 21, 2009

Abstract

We consider the problem of the numerical approximation of the linear controllability of waves. All our experiments are done in a bounded domain Ω of the plane, with Dirichlet boundary conditions and internal control. We use a Galerkin approximation of the optimal control operator of the continuous model, based on the spectral theory of the Laplace operator in Ω. This allows us to obtain surprisingly good illustrations of the main theoretical results available on the controllability of waves, and to formulate some questions for the future analysis of optimal control theory of waves.

*Laboratoire J.-A. Dieudonné, Parc Valrose, Nice, France, lebeau@math.unice.fr
†Institut Universitaire de France
‡Laboratoire J. Kuntzmann, Domaine Universitaire, Grenoble, France, maelle.nodet@inria.fr

Contents

1 Introduction

This paper is devoted to the experimental study of the exact controllability of waves. All our experiments will be done in a bounded domain Ω of the plane, with Dirichlet boundary conditions and with internal control. We use the most natural approach for the numerical computation: a Galerkin approximation of the optimal control operator of the continuous model based on the spectral theory of the Laplace operator in Ω. This will allow us to obtain surprisingly good illustrations of the main theoretical results available on the controllability of waves, and to formulate some questions for the future analysis of the optimal control theory of waves.

The problem of controllability for linear evolution equations and systems has a long story for which we refer to the review of D.-L. Russel in [Rus78] and to the book of J. L. Lions [Lio88]. Concerning controllability of linear waves, the main theoretical result is the so called "Geometric Control Condition" of C. Bardos, G. Lebeau and J. Rauch [BLR92], **GCC** in short, which gives a (almost) necessary and sufficient condition for exact controllability. This is a "geometrical optics" condition on the behavior of optical rays inside $\overline{\Omega}$. Here, optical rays are just straight lines inside Ω, reflected at the boundary according to the Snell-Descartes law of reflection. The precise definition of optical rays near points of tangency with the boundary is given in the works of R. Melrose and J. Sjöstrand [MS78] and [MS82]. For internal control, **GCC** asserts that waves in a regular bounded domain Ω are exactly controllable by control functions supported in the closure of an open sub-domain U and acting during a time T, if (and only if, if one allows arbitrary small perturbations of the time control T and of the control domain U)

GCC: every optical ray of length T in Ω enters the sub-domain U.

Even when **GCC** is satisfied, the numerical computation of the control is not an easy task. The original approach consists first in discretizing the continuous model, and then in computing the control of the discrete system to use it as a numerical approximation of the continuous one. This method has been developed by R. Glowinski et al. (see [GLL90] and [GHL08]), and used for numerical experiments in [AL98]. However, as observed in the first works of R. Glowinski, interaction of waves with a numerical mesh produces spurious high frequency oscillations. In fact, the discrete model is not uniformly exactly controllable when the mesh size goes to zero, since the group velocity converges to zero when the solutions wavelength is comparable to the mesh size. In other words, the processes of numerical discretization and observation or control do not commute. A precise analysis of this lack of commutation and its impact on the computation of the control has been done by E. Zuazua in [Zua02] and [Zua05].

In this paper, we shall use another approach, namely we will discretize the optimal control of the continuous model using a projection of the wave equation onto the finite dimensional space spanned by the eigenfunctions e_j of the Laplace operator in Ω with Dirichlet boundary conditions, $-\triangle e_j = \omega_j^2 e_j, e_j|_{\partial\Omega=0}$, with $\omega_j \leq \omega$. Here, ω will be a cutoff frequency at our disposal. We prove (see lemma 2 in section 2.3) that when **GCC** is satisfied, our numerical control converges when $\omega \to \infty$ to the optimal control of the continuous model . Moreover, when **GCC** is not satisfied, we will do experiments and we will see an exponential blow-up in the cutoff frequency ω of the norm of the discretized optimal control. These blow-up rates will be compared to theoretical results in section 2.3.

The paper is organized as follows.

Section 2 is devoted to the analysis of the optimal control operator for waves in a bounded regular domain of $\mathbb{R}^d$. In section 2.1, we recall the definition of the optimal control operator Λ. In section 2.2, we recall some known theoretical results on Λ: existence, regularity properties and the fact that it preserves the frequency localization. We also state our first conjecture, namely that the optimal control operator Λ is a microlocal operator. In section 2.3, we introduce the spectral Galerkin approximation $M_{T,\omega}^{-1}$ of Λ, where ω is a cutoff frequency. We prove the convergence of $M_{T,\omega}^{-1}$ toward Λ when $\omega \to \infty$, and we analyze the rate of this convergence. We also state our second conjecture on the blow-up rate of $M_{T,\omega}^{-1}$ when **GCC** is not satisfied. Finally, in section 2.4, we introduce the basis of the energy space in which we compute the matrix of the operator $M_{T,\omega}$.

Section 3 is devoted to the experimental validation of our Galerkin approximation. In section 3.1 we introduce the 3 different domains of the plane for our experiments: square, disc and trapezoid. In the first two cases, the geodesic flow is totally integrable and the exact eigenfunctions and eigenvalues of the Laplace operator with Dirichlet boundary condition are known. This is not the case for the trapezoid. In section 3.2 we introduce the two different choices of the control operator we use in our experiments. In the first case (non smooth case), we use $\chi(t,x) = \mathbf{1}_{[0,T]}\mathbf{1}_U$. In the second case (smooth case), we use a suitable regularization of the first case (see formulas (66) and (67)). Perhaps the main contribution of this paper is to give an experimental evidence that the choice of a smooth enough control operator is the right way to get accuracy on control computing. In section 3.3, in the two cases of the square and the disc, we compare the exact eigenvalues with the eigenvalues computed using the 5-points finite difference approximation of the Laplace operator. In section 3.4, formula (69), we define the reconstruction error of our method. Finally, in section 3.5, in the case of the square geometry, we compare the control function (we choose to reconstruct a single eigenvalue) when the eigenvalues and eigenvectors are computed either with finite differences or with exact formulas, and we study the experimental convergence of our numerical optimal control to the exact optimal control of the continuous model when the cutoff frequency goes to infinity.

The last section, 4, presents various numerical experiments which illustrate the theoretical results of section 2, and are in support of our two conjectures. In section 4.1, our experiments illuminate the fact that the optimal control operator preserves the frequency localization, and that this property is far much stronger when the control function is smooth, as predicted by theoretical results. In section 4.2, we use Dirac and box experiments to illustrate the fact that the optimal control operator shows a behavior very close to the behavior of a pseudo-differential operator: this is in support of our first conjecture. In section 4.3, we plot the reconstruction error as a function of the cutoff frequency: this illuminates how the rate of convergence of the Galerkin approximation depends on the regularity of the control function. In section 4.4, we present various results on the energy of the control function. In section 4.5, we compute the condition number of the matrix $M_{T,\omega}$ for a given control domain U, as a function of the control time T and the cutoff frequency ω. In particular, figures 31 and 32 are in support of our second conjecture on the blow-up rate of $M_{T,\omega}^{-1}$ when **GCC** is not satisfied. In section 4.6, we perform experiments in the disc when **GCC** is not satisfied, for two different data: in the first case, every optical rays of length T starting at a point where the data is not small enters the control domain U, and we observe a rather good reconstruction error if the cutoff frequency is not too high. In the second case, there exists an optical ray starting at a point where the data is not small and which never enters the control domain, and we observe a very poor reconstruction at any cutoff frequency. This is a fascinating phenomena which has not been previously studied in theoretical works. It will be of major practical interest to get quantitative results on the best cutoff frequency which optimizes the reconstruction error (this optimal cutoff frequency is equal to ∞ when **GCC** is satisfied, the reconstruction error being equal to 0 in that case), and to estimate the reconstruction error at the optimal cutoff frequency. Clearly, our experiments indicate that a weak Geometric Control Condition associated to the data one wants to reconstruct will enter in such a study.

2 The analysis of the optimal control operator

2.1 The optimal control operator

Here we recall the basic facts we will need in our study of the optimal control operator for linear waves. For more details on the HUM method, we refer to the book of J.-L. Lions [Lio88].

In the framework of the wave equation in a bounded open subset Ω of $\mathbb{R}^d$ with boundary Dirichlet condition, and for internal control the problem of controllability is stated in the following way. Let T be a positive time, U a non void open subset of Ω, and $\chi(t,x)$ as follows:

$$\chi(t,x) = \psi(t)\chi_0(x) \tag{1}$$

where χ_0 is a real L^∞ function on $\overline{\Omega}$, such that support$(\chi_0) = \overline{U}$ and $\chi_0(x)$ is continuous and positive for $x \in U$, $\psi \in C^\infty([0,T])$ and $\psi(t) > 0$

on $]0,T[$. For a given $f=(u_0,u_1)\in H_0^1(\Omega)\times L^2(\Omega)$, the problem is to find a source $v(t,x)\in L^2(0,T;L^2(\Omega))$ such that the solution of the system

$$\begin{cases} \Box u = \chi v \quad \text{in }]0,+\infty[\times\Omega \\ u_{|\partial\Omega}=0, \quad t>0 \\ (u|_{t=0},\partial_t u|_{t=0})=(0,0) \end{cases} \tag{2}$$

reaches the state $f=(u_0,u_1)$ at time T. We first rewrite the wave operator in (2) as a first order system. Let A be the matrix

$$iA=\begin{pmatrix} 0 & Id \\ \triangle & 0 \end{pmatrix} \tag{3}$$

Then A is a unbounded self-adjoint operator on $H=H_0^1(\Omega)\times L^2(\Omega)$, where the scalar product on $H_0^1(\Omega)$ is $\int_\Omega \nabla u \overline{\nabla v} dx$ and $D(A)=\{\underline{u}=(u_0,u_1)\in H,\ A(\underline{u})\in H,\ u_0|_{\partial\Omega}=0\}$. Let $\lambda=\sqrt{-\triangle_D}$ where $-\triangle_D$ is the canonical isomorphism from $H_0^1(\Omega)$ onto $H^{-1}(\Omega)$. Then λ is an isomorphism from $H_0^1(\Omega)$ onto $L^2(\Omega)$. The operator $B(t)$ given by

$$B(t)=\begin{pmatrix} 0 & 0 \\ \chi(t,.)\lambda & 0 \end{pmatrix} \tag{4}$$

is bounded on H, and one has

$$B^*(t)=\begin{pmatrix} 0 & \lambda^{-1}\chi(t,.) \\ 0 & 0 \end{pmatrix} \tag{5}$$

The system (2) is then equivalent to

$$(\partial_t - iA)f = B(t)g, \quad f(0)=0 \tag{6}$$

with $f=(u,\partial_t u)$, $g=(\lambda^{-1}v,0)$. For any $g(t)\in L^1([0,\infty[,H)$, the evolution equation

$$(\partial_t - iA)f = B(t)g, \quad f(0)=0 \tag{7}$$

admits a unique solution $f=S(g)\in C^0([0,+\infty[,H)$ given by the Duhamel formula

$$f(t)=\int_0^t e^{i(t-s)A}B(s)g(s)ds \tag{8}$$

Let $T>0$ be given. Let $\mathcal{R}_T$ be the reachable set at time T

$$\mathcal{R}_T=\{f\in H,\ \exists g\in L^2([0,T],H),\ f=S(g)(T)\} \tag{9}$$

Then $\mathcal{R}_T$ is a linear subspace of H, and is the set of states of the system that one can reach in time T, starting from rest, with the action of an L^2 source g filtered by the control operator B. The control problem consists in giving an accurate description of $\mathcal{R}_T$, and exact controllability is equivalent to the equality $\mathcal{R}_T=H$. Let us recall some basic facts.

Let $\mathcal{H}=L^2([0,T],H)$. Let $\mathcal{F}$ be the closed subspace of $\mathcal{H}$ spanned by solutions of the adjoint evolution equation

$$\mathcal{F}=\{h\in\mathcal{H},\ (\partial_t - iA^*)h=0,\ h(T)=h_T\in H\} \tag{10}$$

Observe that, in our context, $A^* = A$, and the function h in (10) is given by $h(t) = e^{-i(T-t)A}h_T$. Let $\mathcal{B}^*$ be the adjoint of the operator $g \mapsto S(g)(T)$. Then $\mathcal{B}^*$ is the bounded operator from H into $\mathcal{H}$ defined by

$$\mathcal{B}^*(h_T)(t) = B^*(t)e^{-i(T-t)A}h_T \tag{11}$$

For any $g \in L^2([0,T],H)$, one has, with $f_T = S(g)(T)$ and $h(s) = e^{-i(T-s)A}h_T$ the fundamental identity

$$(f_T|h_T)_H = \int_0^T (B(s)g(s)|h(s))ds = (g|\mathcal{B}^*(h_T))_{\mathcal{H}} \tag{12}$$

From (12), one gets easily that the following holds true

$$\mathcal{R}_T \text{ is a dense subspace of } H \iff \mathcal{B}^* \text{ is an injective operator} \tag{13}$$

which shows that approximate controllability is equivalent to a uniqueness result on the adjoint equation. Moreover, one gets from (12), using the Riesz and closed graph theorems, that the following holds true

$$\mathcal{R}_T = H \qquad \iff \exists C, \quad \|h\| \leq C\|\mathcal{B}^*h\| \quad \forall h \in H \tag{14}$$

This is an observability inequality, and $\mathcal{B}^*$ is called the observability operator. We rewrite the observability inequality (14) in a more explicit form

$$\exists C, \quad \|h\|_H^2 \leq C\int_0^T \|B^*(s)e^{-i(T-s)A}h\|_H^2 ds \quad \forall h \in H \tag{15}$$

Assuming that (15) holds true, then $\mathcal{R}_T = H$, $\mathrm{Im}(\mathcal{B}^*)$ is a closed subspace of $\mathcal{H}$, and $\mathcal{B}^*$ is an isomorphism of H onto $\mathrm{Im}(\mathcal{B}^*)$. For any $f \in H$, let $\mathcal{C}_f$ be the set of control functions g driving 0 to f in time T

$$\mathcal{C}_f = \left\{ g \in L^2([0,T],H), \quad f = \int_0^T e^{i(T-s)A}B(s)g(s)ds \right\} \tag{16}$$

From (12), one gets

$$\mathcal{C}_f = g_0 + (\mathrm{Im}\mathcal{B}^*)^\perp, \quad g_0 \in \mathrm{Im}\mathcal{B}^* \cap \mathcal{C}_f \tag{17}$$

and $g_0 = \mathcal{B}^*h_T$ is the optimal control in the sense that

$$\min\{\|g\|_{L^2([0,T],H)},\ g \in \mathcal{C}_f\} \quad \text{is achieved at } g = g_0 \tag{18}$$

Let $\Lambda : H \to H$, $\Lambda(f) = h_T$ be the control map, so that the optimal control g_0 is equal to $g_0(t) = B^*(t)e^{-i(T-t)A}\Lambda(f)$. Then Λ is exactly the inverse of the map $M_T : H \to H$ with

$$\begin{aligned} M_T &= \int_0^T m(T-t)dt = \int_0^T m(s)ds \\ m(s) &= e^{isA}B(T-s)B^*(T-s)e^{-isA^*} \end{aligned} \tag{19}$$

Observe that $m(s) = m^*(s)$ is a bounded, self-adjoint, non-negative operator on H. Exact controllability is thus equivalent to

$$\exists C > 0, \quad M_T = \int_0^T e^{i(T-t)A}\begin{pmatrix} 0 & 0 \\ 0 & \chi^2(t,.) \end{pmatrix} e^{-i(T-t)A}dt \geq C Id \tag{20}$$

With $\Lambda = M_T^{-1}$, the optimal control is then given by $g_0(t) = B^*(t)e^{-i(T-t)A}\Lambda(f)$ and is by (5) of the form $g_0 = (\lambda^{-1}\chi\partial_t w, 0)$ where $w(t) = e^{-i(T-t)A}\Lambda(f)$ is the solution of

$$\begin{cases} \Box w = 0 \quad \text{in } \mathbb{R} \times \Omega, \quad w_{|\partial\Omega} = 0 \\ (w(T,.), \partial_t w(T,.)) = \Lambda(f) \end{cases} \tag{21}$$

Thus, the optimal control function v in (2) is equal to $v = \chi\partial_t w$, where w is the solution of the dual problem (21). The operator $\Lambda = M_T^{-1}$, with M_T given by (20) is called the optimal control operator.

2.2 Theoretical results

In this section we recall some theoretical results on the analysis of the optimal control operator Λ. We will assume here that Ω is a bounded open subset of $\mathbb{R}^d$ with smooth boundary $\partial\Omega$, and that any straight line in $\mathbb{R}^d$ has only finite order of contacts with the boundary. In that case, optical rays are uniquely defined. See an example of such rays in figure 1.

[Figure 1 about here.]

Let $M = \Omega \times \mathbb{R}_t$. The phase space is

$$^bT^*M = T^*\overline{M} \setminus T^*_{\partial M} \simeq T^*M \cup T^*\partial M.$$

The characteristic variety of the wave operator is the closed subset Σ of $^bT^*M$ of points (x, t, ξ, τ) such that $|\tau| = |\xi|$ when $x \in \Omega$ and $|\tau| \geq |\xi|$ when $x \in \partial\Omega$. Let $^bS^*\overline{\Omega}$ be the set of points

$$^bS^*\overline{\Omega} = \{(x_0, \xi_0), \text{ with } |\xi_0| = 1 \text{ if } x_0 \in \Omega, |\xi_0| \leq 1 \text{ if } x_0 \in \partial\Omega\}$$

For $\rho_0 = (x_0, \xi_0) \in {}^bS^*\overline{\Omega}$, and $\tau = \pm 1$, we shall denote by $s \to (\gamma_{\rho_0}(s), t - s\tau, \tau), s \in \mathbb{R}$ the generalized bicharacteristic ray of the wave operator, issued from (x_0, ξ_0, t, τ). For the construction of the Melrose-Sjöstrand flow, we refer to [MS78], [MS82] and to [Hör85], vol 3, chapter XXIV . Then $s \to \gamma_{\rho_0}(s) = (x(\rho_0, s), \xi(\rho_0, s))$ is the optical ray starting at x_0 in the direction ξ_0. When $x_0 \in \partial\Omega$ and $|\xi_0| < 1$, then the right (respectively left) derivative of $x(\rho_0, s)$ at $s = 0$ is equal to the unit vector in $\mathbb{R}^d$ which projects on $\xi_0 \in T^*\partial\Omega$ and which points inside (respectively outside) Ω. In all other cases, $x(\rho_0, s)$ is derivable at $s = 0$ with derivative equal to ξ_0.

We first recall the theorem of [BLR92], which gives the existence of the operator Λ:

Theorem 1 *If the geometric control condition* **GCC** *holds true, then M_T is an isomorphism.*

Next, we recall some new theoretical results obtained in [DL09]. For these results, the choice of the control function $\chi(t, x)$ in (1) will be essential.

Definition 1 *The control function $\chi(t, x) = \psi(t)\chi_0(x)$ is* smooth *if $\chi_0 \in C^\infty(\overline{\Omega})$ and $\psi(t)$ is flat at $t = 0$ and $t = T$.*

For $s \in \mathbb{R}$, we denote by $H^s(\Omega, \triangle)$ the domain of the operator $(-\triangle_{\text{Dirichlet}})^{s/2}$. One has $H^0(\Omega, \triangle) = L^2(\Omega)$, $H^1(\Omega, \triangle) = H_0^1(\Omega)$, and if $(e_j)_{j \geq 1}$ is an L^2 orthonormal basis of eigenfunctions of $-\triangle$ with Dirichlet boundary conditions, $-\triangle e_j = \omega_j^2 e_j$, $0 < \omega_1 \leq \omega_2 \leq ...$, one has

$$H^s(\Omega, \triangle) = \{f \in \mathcal{D}'(\Omega), f = \sum_j f_j e_j,\ \sum_j \omega_j^{2s} |f_j|^2 < \infty\} \tag{22}$$

The following result of [DL09] says that, under the hypothesis that the control function $\chi(t, x)$ is smooth, the optimal control operator Λ preserves the regularity:

Theorem 2 *Assume that the geometric control condition* **GCC** *holds true, and that the control function $\chi(t, x)$ is smooth. Then the optimal control operator Λ is an isomorphism of $H^{s+1}(\Omega, \Delta) \oplus H^s(\Omega, \Delta)$ for all $s \geq 0$.*

Observe that theorem 1 is a particular case of theorem 2 with $s = 0$. In our experimental study, we will see in section 4.3 that the regularity of the control function $\chi(t, x)$ is not only a nice hypothesis to get theoretical results. It is also very efficient to get accuracy in the numerical computation of the control function. In other words, the usual choice of the control function $\chi(t, x) = \mathbf{1}_{[0,T]} \mathbf{1}_U$ is a very poor idea to compute a control.

The next result says that the optimal control operator Λ preserves the frequency localization. To state this result we briefly introduce the material needed for the Littlewood-Paley decomposition. Let $\phi \in C^\infty([0, \infty[)$, with $\phi(x) = 1$ for $|x| \leq 1/2$ and $\phi(x) = 0$ for $|x| \geq 1$. Set $\psi(x) = \phi(x) - \phi(2x)$. Then $\psi \in C_0^\infty(\mathbb{R}^*)$, ψ vanishes outside $[1/4, 1]$, and one has

$$\phi(s) + \sum_{k=1}^{\infty} \psi(2^{-k} s) = 1, \qquad \forall s \in [0, \infty[$$

Set $\psi_0(s) = \phi(s)$ and $\psi_k(s) = \psi(2^{-k} s)$ for $k \geq 1$. We then define the spectral localization operators $\psi_k(D)$, $k \in \mathbb{N}$, in the following way: for $u = \sum_j a_j e_j$, we define

$$\psi_k(D) u = \sum_j \psi_k(\omega_j) a_j e_j \tag{23}$$

One has $\sum_k \psi_k(D) = Id$ and $\psi_i(D)\psi_j(D) = 0$ for $|i - j| \geq 2$. In addition, we introduce

$$S_k(D) = \sum_{j=0}^{k} \psi_j(D) = \psi_0(2^{-k} D), \qquad k \geq 0 \tag{24}$$

Obviously, the operators $\psi_k(D)$ and $S_k(D)$ acts as bounded operators on $H = H_0^1 \times L^2$. The spectral localization result of [DL09] reads as follows.

Theorem 3 *Assume that the geometric control condition* **GCC** *holds true, and that the control function $\chi(t, x)$ is smooth. There exists $C > 0$ such that for every $k \in \mathbb{N}$, the following inequality holds true*

$$\begin{aligned} \|\psi_k(D)\Lambda - \Lambda\psi_k(D)\|_H \leq C2^{-k} \\ \|S_k(D)\Lambda - \Lambda S_k(D)\|_H \leq C2^{-k} \end{aligned} \tag{25}$$

Theorem 3 states that the optimal control operator Λ, up to lower order terms, acts individually on each frequency block of the solution. For instance, if e_n is the n-th eigenvector of the orthonormal basis of $L^2(\Omega)$, if one drives the data $(0, 0)$ to $(e_n, 0)$ in (2) using the optimal control, both the solution u and control v in equation (2) will essentially live at frequency ω_n for n large. We shall do experiments on this fact in section 4.1, and we will clearly see the impact of the regularity of the control function $\chi(t, x)$ on the accuracy of the frequency localization of the numerical control.

Since by the above results the optimal control operator Λ preserves the regularity and the frequency localization, it is very natural to expect that Λ is in fact a micro-local operator, and in particular preserves the wave front set. For an introduction to micro-local analysis and pseudo-differential calculus, we refer to [Tay81] and [Hör85]. In [DL09], it is proved that the optimal control operator Λ for waves on a compact Riemannian manifold without boundary is in fact an elliptic 2×2 matrix of pseudo-differential operators. This is quite an easy result, since if $\chi(t, x)$ is smooth the Egorov theorem implies that the operator M_T given by (20) is a 2×2 matrix of pseudo-differential operators. Moreover, the geometric control condition **GCC** implies easily that M_T is elliptic. Since M_T is self adjoint, the fact that M_T is an isomorphism follows then from $Ker(M_T) = \{0\}$, which is equivalent to the injectivity of $\mathcal{B}^*$. This is proved in [BLR92] as a consequence of the uniqueness theorem of Calderon for the elliptic second order operator $\triangle$. Then it follows that its inverse $\Lambda = M_T^{-1}$ is an elliptic pseudo-differential operator.

In our context, for waves in a bounded regular open subset Ω of $\mathbb{R}^d$ with boundary Dirichlet condition, the situation is far much complicated, since there is no Egorov theorem in the geometric setting of a manifold with boundary. In fact, the Melrose-Sjöstrand theorem [MS78], [MS82] on propagation of singularities at the boundary (see also [Hör85], vol 3, chapter XXIV for a proof) implies that the operator M_T given by (20) is a microlocal operator, but this is not sufficient to imply that its inverse Λ is micro-local. However let $\rho_0 = (x_0, \xi_0) \in T^*\Omega, |\xi_0| = 1$ be a point in the cotangent space such that the two optical rays defined by the Melrose-Sjöstrand flow (see [MS78], [MS82]) $s \in [0, T] \to \gamma_{\pm\rho_0}(s) = (x(\pm\rho_0, s), \xi(\pm\rho_0, s))$, with $\pm\rho_0 = (x_0, \pm\xi_0)$, starting at x_0 in the directions $\pm\xi_0$ have only transversal intersections with the boundary. Then it is not hard to show using formula (20) and the parametrix of the wave operator, inside Ω and near transversal reflection points at the boundary $\partial\Omega$, as presented in figure 2, that M_T is microlocally at ρ_0 an elliptic 2×2 matrix of elliptic pseudo-differential operators.

[Figure 2 about here.]

More precisely, let J be the isomorphism from $H_0^1 \oplus L^2$ on $L^2 \oplus L^2$ given by

$$J = \frac{1}{2}\begin{pmatrix} \lambda & -i \\ \lambda & i \end{pmatrix} \tag{26}$$

One has $2\|J\underline{u}\|^2_{L^2\oplus L^2} = \|\underline{u}\|^2_{H_0^1\oplus L^2}$, and if $u(t,x)$ is the solution of the wave operator $\Box u = 0$ with Dirichlet boundary conditions on $\partial\Omega$, and Cauchy data at time t_0 equal to (u_0, u_1), then one has

$$\begin{array}{rl} \lambda u(t,.) = & \lambda \cos((t-t_0)\lambda)u_0 + \sin((t-t_0)\lambda)u_1 \\ = & e^{i(t-t_0)\lambda}\left(\frac{\lambda u_0 - iu_1}{2}\right) + e^{-i(t-t_0)\lambda}\left(\frac{\lambda u_0 + iu_1}{2}\right) \end{array} \tag{27}$$

so the effect of the isomorphism J is to split the solution $u(t,x)$ into a sum of two waves with positive and negative temporal frequency. Moreover, one has

$$Je^{itA}J^{-1} = \begin{pmatrix} e^{it\lambda} & 0 \\ 0 & e^{-it\lambda} \end{pmatrix} \tag{28}$$

Then JM_TJ^{-1} acts as a non negative self-adjoint operator on $L^2 \oplus L^2$, and is equal to

$$\begin{array}{rl} JM_TJ^{-1} = & \frac{1}{2}\begin{pmatrix} Q_+ & -\mathcal{T} \\ -\mathcal{T}^* & Q_- \end{pmatrix} \\ Q_\pm = & \int_0^T e^{\pm is\lambda}\chi^2(T-s,.)e^{\mp is\lambda}ds \\ \mathcal{T} = & \int_0^T e^{is\lambda}\chi^2(T-s,.)e^{is\lambda}ds \end{array} \tag{29}$$

From (29), using the parametrix of the wave operator, inside Ω and near transversal reflection points at the boundary $\partial\Omega$, and integration by parts to show that $\mathcal{T}$ is a smoothing operator, it is not difficult to get that JM_TJ^{-1} is microlocally at $\rho_0 \in T^*\Omega$ a pseudo-differential operator of order zero with principal symbol

$$\begin{array}{c} \sigma_0(JM_TJ^{-1})(\rho_0) = \frac{1}{2}\begin{pmatrix} q_+(x_0,\xi_0) & 0 \\ 0 & q_-(x_0,\xi_0) \end{pmatrix} \\ q_\pm(x_0,\xi_0) = \int_0^T \chi^2(T-s, x(\pm\rho_0, s))ds \end{array} \tag{30}$$

Obviously, condition (GCC) guarantees that $\sigma_0(JM_TJ^{-1})(\rho_0)$ is elliptic, and therefore $J\Lambda J^{-1}$ will be at ρ_0 a pseudo-differential operator of order zero with principal symbol

$$\sigma_0(J\Lambda J^{-1})(\rho_0) = 2\begin{pmatrix} q_+^{-1}(x_0,\xi_0) & 0 \\ 0 & q_-^{-1}(x_0,\xi_0) \end{pmatrix} \tag{31}$$

Therefore, the only difficulty in order to prove that Λ is a microlocal operator is to get a precise analysis of the structure of the operator M_T near rays which are tangent to the boundary. Since the set of $\rho \in^b S^*\overline{\Omega}$ for which the optical ray $\gamma_\rho(s)$ has only transversal points of intersection with the boundary is dense in $T^*\overline{\Omega} \setminus T^*_{\partial\Omega}$ (see [Hör85]), it is not surprising that our numerical experiments in section 4.2 (where we compute the optimal control associated to a Dirac mass $\delta_{x_0}, x_0 \in \Omega$), confirms the following conjecture:

Conjecture 1 *Assume that the geometric control condition* **GCC** *holds true, that the control function $\chi(t,x)$ is smooth, and that the optical rays have no infinite order of contact with the boundary. Then Λ is a microlocal operator.*

Of course, part of the difficulty is to define correctly what is a microlocal operator in our context. In the above conjecture, microlocal will implies in particular that the optimal control operator Λ preserves the wave front set. A far less precise information is to know that Λ is a microlocal operator at the level of microlocal defect measures, for which we refer to [Gér91]. But this is an easy by-product of the result of N. Burq and G. Lebeau in [BL01].

2.3 The spectral Galerkin method

In this section we describe our numerical approximation of the optimal control operator Λ, and we give some theoretical results on the numerical approximation $M_{T,\omega}$ of the operator M_T given by (20), even in the case where the geometric control condition **GCC** is not satisfied.

For any cutoff frequency ω, we denote by Π_ω the orthogonal projection, in the Hilbert space $L^2(\Omega)$, on the finite dimensional linear subspace L^2_ω spanned by the eigenvectors e_j for $\omega_j \leq \omega$. By the Weyl formula, if c_d denotes the volume of the unit ball in $\mathbb{R}^d$, one has

$$N(\omega) = \dim(L^2_\omega) \simeq (2\pi)^{-d}\mathrm{Vol}(\Omega)c_d\omega^d \quad (\omega \to +\infty) \tag{32}$$

Obviously, Π_ω acts on $H = H^1_0 \times L^2$ and commutes with e^{itA}, λ and J. We define the Galerkin approximation $M_{T,\omega}$ of the operator M_T as the operator on $L^2_\omega \times L^2_\omega$

$$M_{T,\omega} = \Pi_\omega M_T \Pi_\omega = \int_0^T e^{i(T-t)A}\Pi_\omega \begin{pmatrix} 0 & 0 \\ 0 & \chi^2(t,.) \end{pmatrix} \Pi_\omega e^{-i(T-t)A} dt \tag{33}$$

Obviously, the matrix $M_{T,\omega}$ is symmetric and non negative for the Hilbert structure induced by H on $L^2_\omega \times L^2_\omega$, and by (19) one has with $n_\omega(t) = B^*(t)\Pi_\omega e^{-i(T-t)A}$

$$M_{T,\omega} = \int_0^T n^*_\omega(t) n_\omega(t) dt \tag{34}$$

By (29) one has also

$$\begin{aligned} JM_{T,\omega}J^{-1} &= \frac{1}{2}\begin{pmatrix} Q_{+,\omega} & -\mathcal{T}_\omega \\ -\mathcal{T}^*_\omega & Q_{-,\omega} \end{pmatrix} \\ Q_{\pm,\omega} &= \int_0^T e^{\pm is\lambda}\Pi_\omega \chi^2(T-s,.)\Pi_\omega e^{\mp is\lambda} ds \\ \mathcal{T}_\omega &= \int_0^T e^{is\lambda}\Pi_\omega \chi^2(T-s,.)\Pi_\omega e^{is\lambda} ds \end{aligned} \tag{35}$$

Let us first recall two easy results. For convenience, we recall here the proof of these results. The first result states that the matrix $M_{T,\omega}$ is always invertible.

Lemma 1 *For any (non zero) control function $\chi(t,x)$, the matrix $M_{T,\omega}$ is invertible.*

Proof. Let $u = (u_0, u_1) \in L^2_\omega \times L^2_\omega$ such that $M_{T,\omega}(u) = 0$. By (34) one has

$$0 = (M_{T,\omega}(u)|u)_H = \int_0^T \|n_\omega(t)(u)\|_H^2 dt.$$

This implies $n_\omega(t)(u) = 0$ for almost all $t \in]0, T[$. If $u(t, x)$ is the solution of the wave equation with Cauchy data (u_0, u_1) at time T, we thus get by (5) and (1) $\psi(t)\chi_0(x)\partial_t u(t, x) = 0$ for $t \in [0, T]$, and since $\psi(t) > 0$ on $]0, T[$ and $\chi_0(x) > 0$ on U, we get $\partial_t u(t, x) = 0$ on $]0, T[\times U$. One has $u_0 = \sum_{\omega_j \leq \omega} a_j e_j(x)$, $u_1 = \sum_{\omega_j \leq \omega} b_j e_j(x)$ and

$$\partial_t u(t, x) = \sum_{\omega_j \leq \omega} \omega_j a_j \sin((T - t)\omega_j) e_j(x) + \sum_{\omega_j \leq \omega} b_j \cos((T - t)\omega_j) e_j(x)$$

Thus we get $\sum_{\omega_j \leq \omega} \omega_j a_j e_j(x) = \sum_{\omega_j \leq \omega} b_j e_j(x) = 0$ for $x \in U$, which implies, since the eigenfunctions e_j are analytic in Ω, that $a_j = b_j = 0$ for all j. $\square$

For any $\omega_0 \leq \omega$, we define $\Pi_\omega^\perp = 1 - \Pi_\omega$, and we set

$$\begin{aligned} \|\Pi_\omega^\perp \Lambda \Pi_{\omega_0}\|_H &= r_\Lambda(\omega, \omega_0) \\ \|\Pi_\omega^\perp M_T \Pi_{\omega_0}\|_H &= r_M(\omega, \omega_0) \end{aligned} \tag{36}$$

Since the ranges of the operators $\Lambda\Pi_{\omega_0}$ and $M_T\Pi_{\omega_0}$ are finite dimensional vector spaces, one has for any ω_0

$$\begin{aligned} \lim_{\omega \to \infty} r_\Lambda(\omega, \omega_0) &= 0 \\ \lim_{\omega \to \infty} r_M(\omega, \omega_0) &= 0 \end{aligned} \tag{37}$$

The second result states that when **GCC** holds true, the inverse matrix $M_{T,\omega}^{-1}$ converges in the proper sense to the optimal control operator Λ when the cutoff frequency ω goes to infinity.

Lemma 2 *Assume that the geometric condition* **GCC** *holds true. There exists $c > 0$ such that the following holds true: for any given $f \in H$, let $g = \Lambda(f)$, $f_\omega = \Pi_\omega f$ and $g^\omega = M_{T,\omega}^{-1}(f_\omega)$. Then, one has*

$$\|g - g^\omega\|_H \leq c\|f - f_\omega\|_H + \|\Lambda(f_\omega) - M_{T,\omega}^{-1}(f_\omega)\|_H \tag{38}$$

with

$$\lim_{\omega \to \infty} \|\Lambda(f_\omega) - M_{T,\omega}^{-1}(f_\omega)\|_H = 0 \tag{39}$$

Proof. Since **GCC** holds true, there exists $C > 0$ such that one has by (20) $(M_T u|u)_H \geq C\|u\|_H^2$ for all $u \in H$, hence $(M_{T,\omega} u|u)_H \geq C\|u\|_H^2$ for all $u \in L^2_\omega \times L^2_\omega$. Thus, with $c = C^{-1}$, one has $\|\Lambda\|_H \leq c$ and $\|M_{T,\omega}^{-1}\|_H \leq c$ for all ω. Since $g - g^\omega = \Lambda(f - f_\omega) + \Lambda(f_\omega) - M_{T,\omega}^{-1} f_\omega$, (38) holds true. Let us prove that (39) holds true. With $\Lambda_\omega = \Pi_\omega \Lambda \Pi_\omega$, one has

$$\Lambda(f_\omega) - M_{T,\omega}^{-1}(f_\omega) = \Pi_\omega^\perp \Lambda(f_\omega) + (\Lambda_\omega - M_{T,\omega}^{-1}) f_\omega \tag{40}$$

Set for $\omega_0 \leq \omega$, $f_{\omega_0,\omega} = (\Pi_\omega - \Pi_{\omega_0})f$. Then one has

$$\begin{aligned} \|\Pi_\omega^\perp \Lambda(f_\omega)\|_H &= \|\Pi_\omega^\perp \Lambda \Pi_{\omega_0}(f) + \Pi_\omega^\perp \Lambda(f_{\omega_0,\omega})\|_H \\ &\leq r_\Lambda(\omega,\omega_0)\|f\|_H + c\|f_{\omega_0,\omega}\|_H \end{aligned} \tag{41}$$

On the other hand, one has

$$\begin{aligned} (\Lambda_\omega - M_{T,\omega}^{-1})f_\omega &= M_{T,\omega}^{-1}(\Pi_\omega M_T \Pi_\omega^2 \Lambda - \Pi_\omega)f_\omega \\ &= M_{T,\omega}^{-1}(\Pi_\omega M_T \Pi_\omega - \Pi_\omega M_T)\Lambda f_\omega \\ &= -M_{T,\omega}^{-1}\Pi_\omega M_T \Pi_\omega^\perp \Lambda \Pi_\omega f \end{aligned} \tag{42}$$

From (42) we get

$$\|(\Lambda_\omega - M_{T,\omega}^{-1})f_\omega\|_H \leq c\|M_T\|(\|\Lambda\|\|f_{\omega_0,\omega}\|_H + r_\Lambda(\omega,\omega_0)\|f\|_H) \tag{43}$$

Thus, for all $\omega_0 \leq \omega$, we get from (41), (43), and (40)

$$\|\Lambda(f_\omega) - M_{T,\omega}^{-1}(f_\omega)\|_H \leq (1+c\|M_T\|)\Big(r_\Lambda(\omega,\omega_0)\|f\|_H + c\|f_{\omega_0,\omega}\|_H\Big) \tag{44}$$

and (39) follows from (37), (44) and $\|f_{\omega_0,\omega}\|_H \leq \|\Pi_{\omega_0}^\perp f\|_H \to 0$ when $\omega_0 \to \infty$. $\square$

We shall now discuss two important points linked to the previous lemmas. The first point is about the growth of the function

$$\omega \to \|M_{T,\omega}^{-1}\|_H \tag{45}$$

when $\omega \to \infty$. This function is bounded when the geometric control condition **GCC** is satisfied. Let us recall some known results in the general case. For simplicity, we assume that $\partial\Omega$ is an analytic hyper-surface of $\mathbb{R}^d$. We know from [Leb92] that, for $T > T_u$, where $T_u = 2\sup_{x\in\Omega} \mathrm{dist}_\Omega(x,U)$ is the uniqueness time, there exists $A > 0$ such that

$$\limsup_{\omega\to\infty} \frac{\log \|M_{T,\omega}^{-1}\|_H}{\omega} \leq A \tag{46}$$

On the other hand, when there exists $\rho_0 \in T^*\Omega$ such that the optical ray $s \in [0,T] \to \gamma_{\rho_0}(s)$ has only transversal points of intersection with the boundary and is such that $x(\rho_0,s) \notin \overline{U}$ for all $s \in [0,T]$, then **GCC** is not satisfied. Moreover it is proven in [Leb92], using an explicit construction of a wave concentrated near this optical ray, that there exists $B > 0$ such that

$$\liminf_{\omega\to\infty} \frac{\log \|M_{T,\omega}^{-1}\|_H}{\omega} \geq B \tag{47}$$

Our experiments lead us to think that the following conjecture may be true for a "generic" choice of the control function $\chi(t,x)$:

Conjecture 2 *There exists $C(T,U)$ such that*

$$\lim_{\omega\to\infty} \frac{\log \|M_{T,\omega}^{-1}\|_H}{\omega} = C(T,U) \tag{48}$$

In our experiments, we have studied (see section 4.5) the behavior of $C(T,U)$ as a function of T, when the geometric control condition **GCC** is satisfied for the control domain U for $T \geq T_0$. These experiments confirm the conjecture 2 when $T < T_0$. We have not seen any clear change in the behavior of the constant $C(T,U)$ when T is smaller than the uniqueness time T_u.

The second point we shall discuss is the rate of convergence of our Galerkin approximation. By lemma 2, and formulas (43) and (44), this speed of convergence is governed by the function $r_\Lambda(\omega, \omega_0)$ defined in (36). The following lemma tells us that when the control function is smooth, the convergence in (37) is very fast.

Lemma 3 *Assume that the geometric condition* **GCC** *holds true and that the control function $\chi(t,x)$ is smooth. Then there exists a function g with rapid decay such that*

$$r_\Lambda(\omega, \omega_0) \leq g\left(\frac{\omega}{\omega_0}\right) \tag{49}$$

Proof. By theorem 2, the operator $\lambda^s \Lambda \lambda^{-s}$ is bounded on H for all $s \geq 0$. Thus we get, for all $s \geq 0$:

$$\|\Pi_\omega^\perp \Lambda \Pi_{\omega_0}\|_H = \|\Pi_\omega^\perp \lambda^{-s} \lambda^s \Lambda \lambda^{-s} \lambda^s \Pi_{\omega_0}\|_H \leq C_s \left(\frac{\omega_0}{\omega}\right)^s$$

where we have used $\|\lambda^s \Pi_{\omega_0}\|_H \leq \omega_0^s$ and $\|\Pi_\omega^\perp \lambda^{-s}\|_H \leq \omega^{-s}$. The proof of lemma 3 is complete. $\square$

Let us recall that $JM_{T,\omega}J^{-1}$ and the operators $Q_{\pm,\omega}$ and $\mathcal{T}_\omega$ are defined by formula (35). For any bounded operator M on L^2, the matrix coefficients of M in the basis of the eigenvectors e_n are

$$M_{i,j} = (Me_i | e_j) \tag{50}$$

From (1) and (35) one has, for $\omega_i \leq \omega$, $\omega_j \leq \omega$:

$$\begin{aligned} Q_{\pm,\omega,i,j} &= \int_0^T \left(e^{\pm is\lambda} \Pi_\omega \psi^2(T-s) \chi_0^2(x) \Pi_\omega e^{\mp is\lambda}(e_i) | e_j\right) ds \\ &= \int_0^T \psi^2(T-s) e^{\pm is(\omega_j - \omega_i)} \, ds \, \left(\chi_0^2 e_i | e_j\right) \end{aligned}$$

Since $\psi(t) \in C_0^\infty$ has support in $[0,T]$, we get that, for any $k \in \mathbb{N}$, there exists a constant C_k independent of the cutoff frequency ω, such that one has

$$\sup_{i,j} |(\omega_i - \omega_j)^k Q_{\pm,\omega,i,j}| \leq C_k \tag{51}$$

Moreover, by the results of [DL09], we know that the operator $\mathcal{T}$ defined in (29) is smoothing, and therefore we get

$$\sup_{i,j} |(\omega_i + \omega_j)^k |\mathcal{T}_{\omega,i,j} \leq C_k \tag{52}$$

Figure 3 shows the log of $JM_{T,\omega}J^{-1}$ coefficients and illustrates the decay estimates (51) and (52). A zoom in is done in figure 4, so that we can observe more precisely (51). In particular we can notice that the distribution of the coefficients along the diagonal of the matrix is not regular. Figure 5 presents the same zoom for $JM_{T,\omega}^{-1}J^{-1}$. This gives an illustration of the matrix structure of a microlocal operator. Figure 6 represents the log of $JM_{T,\omega}J^{-1}$ coefficients *without smoothing*. And finally, figure 7 gives a view of the convergence of our Galerkin approximation, as it presents the matrix entries of $J(\Lambda_\omega - M_{T,\omega}^{-1})J^{-1}$, illustrating lemma 2, its proof, and lemma 3.

[Figure 3 about here.]

[Figure 4 about here.]

[Figure 5 about here.]

[Figure 6 about here.]

[Figure 7 about here.]

2.4 Computation of the discrete control operator

For any real ω, let $N(\omega) = \sup\{n, \omega_n \leq \omega\}$. Then the dimension of the vector space L^2_ω is equal to $N(\omega)$. Let us define the following $(\phi_j)_{1\leq j\leq 2N(\omega)}$:

$$\left\{ \begin{array}{rll} \phi_j = \frac{e_j}{\omega_j} & \text{for} & 1 \leq j \leq N(\omega) \\ \phi_j = e_{j-N(\omega)} & \text{for} & N(\omega)+1 \leq j \leq 2N(\omega) \end{array} \right. \tag{53}$$

Then $(\phi_j)_{1\leq j\leq 2N(\omega)}$ is an orthonormal basis of the Hilbert space $H_\omega = \Pi_\omega(H^1_0(\Omega) \oplus L^2(\Omega))$.

In this section we compute explicitly $\left(M_T\phi_l|\phi_k\right)_H$ for all $1 \leq k, l \leq 2N(\omega)$. We recall

$$\begin{array}{rcl} e^{isA}\begin{bmatrix} e_i \\ 0 \end{bmatrix} & = & \begin{bmatrix} \cos(s\omega_i)e_i(x) \\ -\omega_i \sin(s\omega_i)e_i(x) \end{bmatrix} \\ e^{isA}\begin{bmatrix} 0 \\ e_i \end{bmatrix} & = & \begin{bmatrix} \sin(s\omega_i)e_i(x)/\omega_i \\ \cos(s\omega_i)e_i(x) \end{bmatrix} \end{array} \tag{54}$$

We now compute the coefficients of the M_T matrix, namely $M_{T\,n,m} = \left(M_T\phi_n|\phi_m\right)_H$:

$$\begin{array}{rcl} M_{T\,n,m} & = & \left(M_T\phi_n|\phi_m\right)_H \\ & = & \int_0^T \left(e^{isA}BB^*e^{-isA}\phi_n|\phi_m\right)_H dt \\ & = & \int_0^T \left(\begin{pmatrix} 0 & 0 \\ 0 & \chi^2 \end{pmatrix} e^{-isA}\phi_n | e^{-isA}\phi_m\right)_H dt \end{array} \tag{55}$$

We now have to distinguish four cases, depending on m, n being smaller or larger than $N(\omega)$. For the case $(m,n) \le N(\omega)$ we have:

$$
\begin{aligned}
M_{T\,n,m} &= \int_0^T \left(\begin{pmatrix} 0 & 0 \\ 0 & \chi^2 \end{pmatrix} e^{-isA}\phi_n | e^{-isA}\phi_m \right)_H ds \\
&= \int_0^T \left(\begin{pmatrix} 0 & 0 \\ 0 & \chi^2 \end{pmatrix} \begin{bmatrix} \cos(s\omega_n) f_n(x) \\ \omega_n \sin(s\omega_n) f_n(x) \end{bmatrix} | \begin{bmatrix} \cos(s\omega_m) f_m(x) \\ \omega_m \sin(s\omega_m) f_m(x) \end{bmatrix} \right)_H ds \\
&= \int_0^T \left(\begin{bmatrix} 0 \\ \omega_n \chi^2 \sin(s\omega_n) f_n(x) \end{bmatrix} | \begin{bmatrix} \cos(s\omega_n) f_m(x) \\ \omega_m \sin(s\omega_m) f_m(x) \end{bmatrix} \right)_H ds \\
&= \int_0^T ((\psi(t)\chi_0(x))^2 \omega_n \sin(s\omega_n) f_n(x) | \omega_m \sin(s\omega_m) f_m(x))_{L^2(\Omega)} ds \\
&= \int_0^T \psi^2 \sin(s\omega_n) \sin(s\omega_m)\, ds \int_\Omega \chi_0^2 e_n(x) e_m(x)\, dx \\
&= a_{n,m} G_{n,m}
\end{aligned} \tag{56}
$$

where

$$
a_{n,m} = \int_0^T \psi^2 \sin(s\omega_m) \sin(s\omega_n)\, ds \tag{57}
$$

and

$$
G_{n,m} = \int_\Omega \chi_0^2(x)\, e_m(x)\, e_n(x)\, dx \tag{58}
$$

Similarly, for the case $n > N(\omega)$, $m \le N(\omega)$ we have:

$$
\begin{aligned}
M_{T\,n,m} &= \int_0^T \left(\begin{pmatrix} 0 & 0 \\ 0 & \chi^2 \end{pmatrix} e^{-isA}\phi_n | e^{-isA}\phi_m \right)_H ds \\
&= \int_0^T \left(\begin{pmatrix} 0 & 0 \\ 0 & \chi^2 \end{pmatrix} \begin{bmatrix} \sin(s\omega_n) f_n(x)/\omega_n \\ \cos(s\omega_n) f_n(x) \end{bmatrix} | \begin{bmatrix} \cos(s\omega_m) f_m(x) \\ \omega_m \sin(s\omega_m) f_m(x) \end{bmatrix} \right)_H ds \\
&= \int_0^T \left(\begin{bmatrix} 0 \\ \chi^2 \cos(s\omega_n) f_n(x) \end{bmatrix} | \begin{bmatrix} \cos(s\omega_n) f_m(x) \\ \omega_m \sin(s\omega_m) f_m(x) \end{bmatrix} \right)_H ds \\
&= \int_0^T (\chi^2 \cos(s\omega_n) f_n(x) | \omega_m \sin(s\omega_m) f_m(x))_{L^2(\Omega)} ds \\
&= \int_0^T \psi^2 \cos(s\omega_n) \sin(s\omega_m)\, ds \int_\Omega \chi_0^2 e_n(x) e_m(x)\, dx \\
&= b_{n,m} G_{n,m}
\end{aligned} \tag{59}
$$

where

$$
b_{n,m} = \int_0^T \psi^2 \cos(s\omega_n) \sin(s\omega_m)\, ds \tag{60}
$$

For $n \le N(\omega)$ and $m > N(\omega)$ we get:

$$
M_{T\,n,m} = c_{n,m} G_{n,m} \tag{61}
$$

where

$$
c_{n,m} = b_{m,n} = \int_0^T \psi^2 \cos(s\omega_m) \sin(s\omega_n)\, ds \tag{62}
$$

And for $m, n > N(\omega)$:

$$
M_{T\,n,m} = d_{n,m} G_{n,m} \tag{63}
$$

where

$$
d_{n,m} = \int_0^T \psi^2 \cos(s\omega_m) \cos(s\omega_n)\, ds \tag{64}
$$

The above integrals have to be implemented carefully when $|\omega_n - \omega_m|$ is small, even when $\psi(t) = 1$.

3 Numerical setup and validation

3.1 Geometries and control domains

The code we implemented allows us to choose the two-dimensional domain Ω, as well as the control domain U. In the sequel, we will present some results with three different geometries: square, disc and trapezoid. For each geometry, we have chosen a reference shape of control domain. It consists of the neighborhood of two adjacent sides of the boundary (in the square), of a radius (in the disc), of the base side (in the trapezoid). Then we adjust the width of the control domain, and also its smoothness (see next paragraph). Figures 8, 9 and 10 present these domains, and their respective control domains, either non-smooth (left panels) or smooth (right panels).

[Figure 8 about here.]

[Figure 9 about here.]

[Figure 10 about here.]

3.2 Time and space smoothing

We will investigate the influence of the regularity of the function $\chi(t, x) = \psi(t)\chi_0(x)$. Different options have been set.

Space-smoothing. The integral (58) defining $G_{n,m}$ features χ_0. In the literature we find $\chi_0 = \mathbf{1}_U$, so that

$$G_{n,m} = \int_U e_n(x)\, e_m(x)\, dx \tag{65}$$

In [DL09] the authors show that a smooth χ_0^2 leads to a more regular control (see also theorem 3 and lemma 3). Thus for each control domain U we implemented both smooth and non-smooth (constant) cases. The different implementations of χ_0 are:

- constant case: $\chi_0(x, y) = \mathbf{1}_U$,
- "smooth" case: $\chi_0(x, y)$ has the same support of U, the width a of the domain $\{x \in \Omega, 0 < \chi_0(x) < 1\}$ is adjustable, and on this domain χ is a polynomial of degree 2. For example, in the square we have:

$$\begin{aligned} \chi_0(x, y) \quad = \quad \mathbf{1}_U \Big[1 - \Big(\mathbf{1}_{x \geq a} + \tfrac{x^2}{a^2} . \mathbf{1}_{x<a} \Big) \\ \Big(\mathbf{1}_{y \leq 1-a} + \tfrac{(1-y)^2}{a^2} . \mathbf{1}_{y>1-a} \Big) \Big] \end{aligned} \tag{66}$$

Time-smoothing. Similarly, the time integrals (57,60,62,64) defining a, b, c and d features $\psi(t)$, which is commonly chosen as $\mathbf{1}_{[0,T]}$. As previously, better results are expected with a smooth $\psi(t)$. In the code, the integrals (57,60,62,64) are computed explicitly, the different implementations of ψ being:

- constant case $\psi = \mathbf{1}_{[0,T]}$,
- "smooth case"

$$\psi(t) = \frac{4t(T-t)}{T^2}\mathbf{1}_{[0,T]} \tag{67}$$

3.3 Validation of the eigenvalues computation

The code we implemented has a wide range of geometries for Ω. As it is a spectral-Galerkin method, it requires the accurate computation of eigenvalues and eigenvectors. We used Matlab *eigs*[1] function. Figure 11 shows the comparison between the first 200 exact eigenvalues in the square, and those computed by Matlab with 500×500 grid-points. Figure 12 presents the same comparison in the disc, for 250 eigenvalues, the "exact" ones being computed as zeros of Bessel function.

[Figure 11 about here.]

[Figure 12 about here.]

3.4 Reconstruction error.

In the sequel, we will denote the input data $u = (u_0, u_1)$, and its image by the control map $w = (w_0, w_1) = \Lambda(u_0, u_1)$, which will often be called the "control". We recall from section 2.1 that for a given data $u = (u_0, u_1)$ to be reconstructed at time T, the optimal control $v(t)$ is given by

$$v(t) = \chi \partial_t e^{-i(T-t)A} w = \chi \partial_t e^{-i(T-t)A} \Lambda(u) \tag{68}$$

Then, solving the wave equations (2) forward, with null initial conditions and χv as a forcing source, we reach $y = (y_0, y_1)$ in time T. Should the experiment be perfect, we would have $(y_0, y_1) = (u_0, u_1)$. The reconstruction error is then by definition:

$$E = \sqrt{\frac{\|u_0 - y_0\|^2_{H^1(\Omega)} + \|u_1 - y_1\|^2_{L^2(\Omega)}}{\|u_0\|^2_{H^1(\Omega)} + \|u_1\|^2_{L^2(\Omega)}}} \tag{69}$$

3.5 Validation for the square geometry

3.5.1 Finite differences versus exact eigenvalues

In this paragraph, we compare various outputs for our spectral method, when the eigenvalues and eigenvectors are computed either with finite-differences or with exact formulas. In this first experiment, we have $N \times$

[1] `www.mathworks.com/access/helpdesk/help/techdoc/ref/eigs.html`

$N = 500 \times 500$ grid-points and we use $N_e = 100$ eigenvalues to compute the G and M_T matrices. The data (u_0, u_1) is as follows:

$$\left\{ \begin{array}{rcl} u_0 & = & e_{50} \\ u_1 & = & 0 \end{array} \right. \tag{70}$$

Where e_n denotes the n-th *exact* eigenvector. The control time T is equal to 3, the control domain U is 0.2 wide, and we do not use any smoothing. For reconstruction we use 2000 eigenvalues and eigenvectors.
Table 1 shows the condition number of the M_T matrices, and reconstruction errors, which are very similar for both experiments.

[Table 1 about here.]

Figure 13 shows the relative reconstruction error between the data u and the reconstructed y for both experiments:

$$\begin{array}{rcl} \text{Relative reconstruction error SP}_n & = & \dfrac{|U_{0,n} - Y^{sp}_{0,n}|}{\|U_0 + U_1\|} \\ \text{Relative reconstruction error FD}_n & = & \dfrac{|U_{0,n} - Y^{fd}_{0,n}|}{\|U_0 + U_1\|} \end{array} \tag{71}$$

and similarly for u_1 and y_1, where $U_{0,n}$ is the n-th spectral coefficient of the data u_0, $Y^{sp}_{0,n}$ is the n-th spectral coefficient (in the basis (ϕ_j) defined by formulas (53) in section 2.4) of the reconstructed y_0 when the control w is obtained thanks to exact eigenvalues and $Y^{fd}_{0,n}$ is the n-th spectral coefficient of y_0 when the control w is obtained thanks to finite differences eigenvalues. The norm $\|U_0 + U_1\|$ in our basis (ϕ_j) is given by:

$$\|U_0 + U_1\|^2 = \sum_{n=1}^{N_e} U^2_{0,n} + U^2_{1,n} \tag{72}$$

For exact eigenvalues, we can see that the errors are negligible on the first 100-th spectral coefficients, and quite small on the next ones. We have similar results for finite differences eigenvalues, except that we have an error on the 50-th coefficient. This error does not occur when the reconstruction is done with the same finite differences eigenvectors basis, and it can probably be explained as follows: to compute the reconstructed y from the finite difference control w, we first compute an approximation of w as a function of (x, y) (i.e. on the grid) from its spectral coefficients (on the finite differences eigenvectors basis), then we compute the coefficients of this function on the exact basis (thanks to a very simple integration formula). We thus introduce two sources of errors, projection on the grid and projection on the exact basis, which do not have anything to do with our spectral Galerkin method. Therefore we will not discuss the matter in further detail here.

[Figure 13 about here.]

3.5.2 Impact of the number of eigenvalues

In this paragraph, we still use the same data (70), but the number of eigenvalues and eigenvectors N_e used to compute the M_T matrices is varying. Table 2 shows M_T condition numbers and reconstruction errors for various N_e with exact or finite-differences-computed eigenvalues. The reconstruction is still performed with 2000 exact eigenvalues. We can see that the finite differences eigenvalues lead to almost as good results as exact eigenvalues. We also observe in both cases the decrease of the reconstruction error with an increasing number of eigenvalues, as predicted in lemma 3. A 5% error is obtained with 70 eigenvalues (the input data being the 50-th eigenvalue), and 100 eigenvalues lead to less than 2%.

[Table 2 about here.]

4 Numerical experiments

4.1 Frequency localization

In this subsection, the geometry (square) as well as the number of eigenvalues used (200 for HUM, 2000 for verification) are fixed. Note also that in this paragraph we use only exact eigenvalues for HUM and verification. The data is also fixed to a given eigenmode, that is:

$$u_0 = e_{50} \quad u_1 = 0 \tag{73}$$

where e_n is the n-th eigenvector of $-\Delta$ on the square.

[Figure 14 about here.]

The first output of interest is the spreading of w spectral coefficients, compared to u. Figure 15 shows the spectral coefficients of the input (u_0, u_1) and the control (w_0, w_1) with and without smoothing. As predicted by theorem 3 and lemma 3 we can see that the main coefficient of (w_0, w_1) is the 50-th of w_0, and also that the smoothing noticeably improves the localization of w.

[Figure 15 about here.]

Similarly we can look at the spectral coefficients of the reconstruction error. Figure 16 presents the reconstruction error (see paragraph 3.4 for a definition) with or without smoothing. We notice that the errors occur mostly above the cutoff frequency (used for $M_{T,\omega}$ computation, and thus for the control computation). Another important remark should be made here: the smoothing has a spectacular impact on the frequency localization of the error, as well as on the absolute value of the error (maximum of 2.10^{-3} without smoothing, and 8.10^{-7} with smoothing), as announced in theorem 3 and lemma 3.

[Figure 16 about here.]

Remark 1 *For other domains, such as the disc and trapezoid, as well as other one-mode input data, we obtain similar results. The results also remain the same if we permute* $u0$ *and* $u1$*, i.e. if we choose* $u0 = 0$ *and* $u1$ *equal to one fixed mode.*

4.2 Space localization

4.2.1 Dirac experiments

In this section we investigate the localization in space. To do so, we use "Dirac" functions $\delta_{(x,y)=(x_0,y_0)}$ as data, or more precisely truncations to a given cutoff frequency of Dirac functions:

$$\begin{cases} u_0 & = & \sum_{i=1}^{N_i} e_n(x_0, y_0)\, e_n \\ u_1 & = & 0 \end{cases} \tag{74}$$

where N_i is the index corresponding to the chosen cutoff frequency, with $N_i = 100$ or 120 in the sequel. Figure 17 shows the data u_0 and the control w_0 in the square with exact eigenvalues, without smoothing, the results being similar with smoothing. We can see that the support of w_0 is very similar to u_0's. Figure 18 presents the reconstruction error associated to this experiment. We can see as before that the smoothing produces highly reduced errors.

[Figure 17 about here.]

[Figure 18 about here.]

Similarly, we performed experiments with numerical approximation of a Dirac function as input data in the disc and in a trapezoid. Figures 19 and 20 present the space-localization of u_0 and w_0 without smoothing (we get similar results with smoothing). As previously, the control w_0 is supported by roughly the same area than the input u_0. In the disc we can see a small disturbance, located in the symmetric area of the support of u_0 with respect to the control domain U. However, this error does not increase with N_i, as we can see in figure 21 (case $N_i = 200$) so it remains compatible with conjecture 1.
Figure 22 shows the reconstruction errors for these experiments, with or without smoothing. As before we notice the high improvement produced by the smoothing. We get similar errors in the trapezoid.

[Figure 19 about here.]

[Figure 20 about here.]

[Figure 21 about here.]

[Figure 22 about here.]

4.2.2 Box experiments in the square

In this paragraph we consider the case $u_0 = \mathbf{1}_{\text{box}}$, where box $= [0.6, 0.8] \times [0.2, 0.4]$ is a box in the square. The control domain U is 0.1 wide: $U = \{x < 0.1 \text{ and } y > 0.9\}$. These experiments were performed in the square with 1000 exact eigenvalues for the M_T matrix computation, the input data u_0 being defined thanks to 800 eigenvalues. Figures 23 and 24 show the space localization of the data u_0 and the control w_0 without and with smoothing. As before we can notice that the space localization is preserved, and that with smoothing the support of w_0 is more sharply defined. Figures 25 and 26 show the reconstruction errors for two different data, the first being the same as in figure 23, and the second being similar but rotated by $\pi/4$. We show here only the case with smoothing, the errors being larger but similarly shaped without. We can notice that the errors lows and highs are located on a lattice whose axes are parallel to the box sides. This is compatible with the structure of the wave-front set associated to both input data.

[Figure 23 about here.]

[Figure 24 about here.]

[Figure 25 about here.]

[Figure 26 about here.]

4.3 Reconstruction error

In this section we investigate lemma 3 or more precisely the subsequent remark **??**. This remark states that the reconstruction error should decrease as the inverse of the cutoff frequency without smoothing, and as the inverse of the fifth power of the cutoff frequency with smoothing. To investigate this, we perform a "one-mode" experiment (see paragraph 4.1) using the 50-th mode as input data. We then compute the control with an increasing cutoff frequency, up to 47 (finite differences case) or 82 (exact case), and we compute the reconstruction error, thanks to a larger cutoff frequency (52 in the finite differences case, or 160 in the exact case).
Figure 27 represents the reconstruction error (with exact or finite differences eigenvalues) as a function of the cutoff frequency (i.e., the largest eigenvalue used for the control function computation). Figure 28 presents the same results (with finite differences eigenvalues only) for two different geometries: the square, and the trapezoid (general domain). The log scale allows us to see that the error actually decreases as the inverse of the cutoff frequency without smoothing, and as the inverse of the fifth power of the cutoff frequency with smoothing, according to remark **??**.

[Figure 27 about here.]

[Figure 28 about here.]

4.4 Energy of the control function

In this paragraph we investigate the impact of the smoothing, the width of the control domain U and the control time T on various outputs such as the condition number of M_T, the reconstruction error $\|u-y\|$, and the norm of the control function $\|w\|$.
To do so we performed several one-mode experiments (see paragraph 4.1,

mode 500) in the square, with exact eigenvalues, 1000 eigenvalues used for computation of M_T, 2000 eigenvalues used for reconstruction and verification. We chose various times: 2.5 and 8, plus their "smoothed" counterparts, according to the empirical formula $T_{\text{smooth}} = 15/8 * T$. This increase of T_{smooth} is justified on the theoretical level by formulas (31) and (30) which show that the efficiency of the control is related to a mean value of $\chi(t,x)$ on the trajectories. Similarly, we chose various width of U: 1/10 and 3/10, plus their "smoothed" counterpart, which are double. Table 3 presents the numerical results for these experiments. This table draws several remarks. First, the condition number of M_T, the reconstruction error and the norm of the control w decrease with increasing time and U. Second, if we compare each non-smooth experiment with its "smoothed" counterpart (the comparison is of course approximate, since the "smoothed" time and width formulas are only reasonable approximations), the condition number seems similar, as well as the norm of the control function w, whereas the reconstruction error is far smaller with smoothing than without.

[Table 3 about here.]

Figures 29 and 30 emphasize the impact of the control time, they present the reconstruction error, the norm of the control, and the condition number of M_T, as a function of the control time (varying between 2.5 and 16), with or without smoothing. Conclusions are similar to the table conclusions.

[Figure 29 about here.]

[Figure 30 about here.]

4.5 Condition number

In this section, we investigate conjecture 2. To do so, we compute the condition number of $M_{T,\omega}$, as we have:

$$\text{cond}(M_{T,\omega}) = \|M_{T,\omega}\|.\|M_{T,\omega}^{-1}\| \simeq \|M_T\|.\|M_{T,\omega}^{-1}\| \tag{75}$$

Figure 31 shows the condition number of the M_T matrix as a function of the control time or of the last eigenvalue used for the control function computation. According to conjecture 2, we obtain lines of the type

$$\log\left(\text{cond}(M_{T,\omega})\right) = \omega.C(T,U) \tag{76}$$

Figure 32 shows for various eigenvalues numbers the following curves:

$$T \mapsto \frac{\log\left(\text{cond}(M_{T,\omega})\right)}{\omega} \tag{77}$$

Similarly, we can draw conclusions compatible with conjecture 2, as these curves seems to converge when the number of eigenvalues grows to infinity.

[Figure 31 about here.]

[Figure 32 about here.]

4.6 Non-controlling domains

In this section we investigate two special experiments with non-controlling domains, i.e. such that the geometric control condition is not satisfied whatever the control time.
First we consider the domain presented in Figure 33.

[Figure 33 about here.]

For this domain the condition number of the M_T matrix is large, and subsequently we should be experiencing difficulties to reconstruct the data u. We perform one-mode experiments with two different eigenvectors, one being localized in the center of the disc (eigenvalue 60), the other being localized around the boundary (eigenvalue 53) as can be seen on Figure 34.

[Figure 34 about here.]

The various outputs are presented in Table 4, and we can see that the inversion is fairly accurate for the 53rd eigenmode, while it is logically poor for the 60th eigenmode. Moreover, the energy needed for the control process, i.e. the norm of the control w, is small for the 53rd eigenvector, while it is large for the 60-th. We can also notice that the smoothing has the noticeable effect to decrease the reconstruction error, the norm of the control function w being similar.

[Table 4 about here.]

In the second experiment we change the point of view: instead of considering one given domain and two different data, we consider one given data, and two different non-controlling domains. The data is again u_{53} (see Figure 34), which is localized at the boundary of the disc. The first domain is the previous one (see Figure 33), the second domain is presented in Figure 35, it is localized at the center of the disc.

[Figure 35 about here.]

In either case, the condition number of the M_T matrix is large, and the data should prove difficult to reconstruct. Table 5 present the outputs we get for the two domains. As previously, we observe that the control process works fairly well for the appropriate control domain, with a small error as well as a small energy for the control. Conversely, when the control domain does not "see" the input data, the results are poorer: the energy needed is large with or without smoothing, the error is also large without smoothing, it is however small with smoothing.

[Table 5 about here.]

Acknowledgement

The experiments have been realized with Matlab[2] software on Laboratoire Jean-Alexandre Dieudonné (Nice) and Laboratoire Jean Kuntzmann

[2]The Mathworks, Inc. `http://www.mathworks.fr`

(Grenoble) computing machines. The INRIA Gforge[3] has also been used. The authors thank J.-M. Lacroix (Laboratoire J.-A. Dieudonné) for his managing of Nice computing machine.
This work has been partially supported by Institut Universitaire de France.

References

[AL98] M. Asch and G. Lebeau. Geometrical aspects of exact boundary controllability of the wave equation. a numerical study. *ESAIM:COCV*, 3:163–212, 1998.

[BL01] N. Burq and G. Lebeau. Mesures de défaut de compacité, application au système de lamé. *Ann. Sci. École Norm. Sup.*, 34(6):817–870, 2001.

[BLR92] C. Bardos, G. Lebeau, and J. Rauch. Sharp sufficient conditions for the observation, control and stabilisation of waves from the boundary. *SIAM J.Control Optim.*, 305:1024–1065, 1992.

[DL09] B. Dehman and G. Lebeau. Analysis of the HUM Control Operator and Exact Controllability for Semilinear Waves in Uniform Time. to appear in SIAM Control and Optimization, 2009.

[Gér91] P. Gérard. Microlocal defect measures. *C.P.D.E*, 16:1762–1794, 1991.

[GHL08] R. Glowinski, J. W. He, and J.-L. Lions. *Exact and Approximate Controllability for Distributed Parameter Systems: A Numerical Approach.* Cambridge University Press, 2008.

[GLL90] R. Glowinski, C.H. Li, and J.L. Lions. A numerical approach to the exact boundary controllability of the wave equation (I). dirichlet controls : description of the numerical methods. *Japan J. Appl. Math.*, 7:1–76, 1990.

[Hör85] L. Hörmander. *The analysis of linear partial differential operators. III.* Grundl. Math. Wiss. Band 274. Springer-Verlag, Berlin, 1985. Pseudodifferential operators.

[Leb92] G. Lebeau. Contrôle analytique I : Estimations a priori. *Duke Math. J.*, 68(1):1–30, 1992.

[Lio88] J.-L. Lions. *Contrôlabilité exacte, perturbations et stabilisation de systèmes distribués. Tome 2*, volume 9 of *Recherches en Mathématiques Appliquées [Research in Applied Mathematics].* Masson, Paris, 1988.

[MS78] R.-B. Melrose and J. Sjostrand. Singularities of boundary value problems I. *CPAM*, 31:593–617, 1978.

[MS82] R.-B. Melrose and J. Sjostrand. Singularities of boundary value problems II. *CPAM*, 35:129–168, 1982.

[Rus78] D.-L. Russell. Controllability and stabilizability theory for linear partial differential equations: recent progress and open questions. *SIAM Rev*, 20:639–739, 1978.

[3] http://gforge.inria.fr

[Tay81] M. Taylor. *Pseudodifferential operators.* Princeton University Press, 1981.

[Zua02] E. Zuazua. Controllability of partial differential equations and its semi-discrete approximations. *Discrete and Continuous Dynamical Systems*, 8(2):469–513, 2002.

[Zua05] E. Zuazua. Propagation, observation, and control of waves approximated by finite difference methods. *SIAM Rev*, 47(2):197–243, 2005.

List of Figures

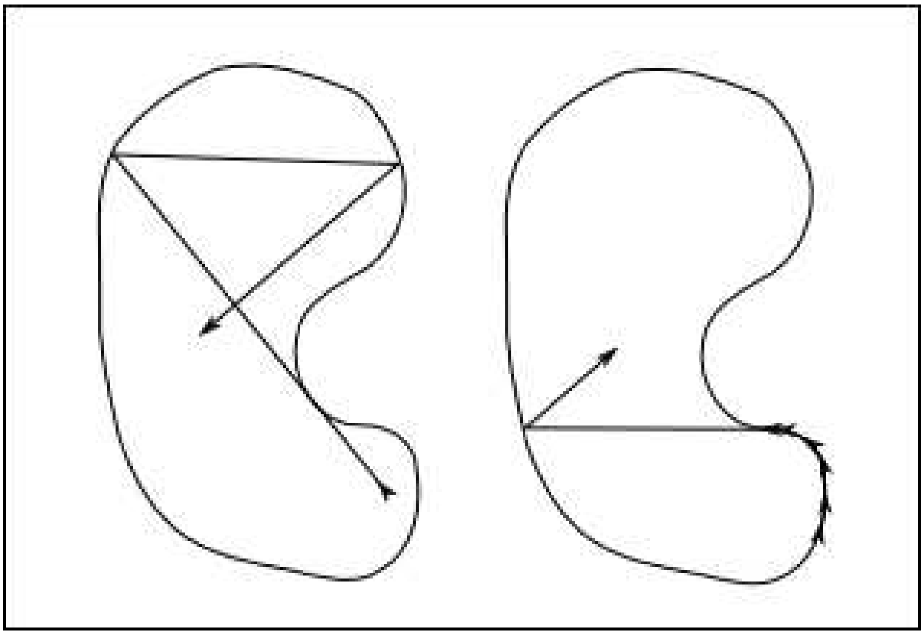

Figure 1: Example of optical rays.

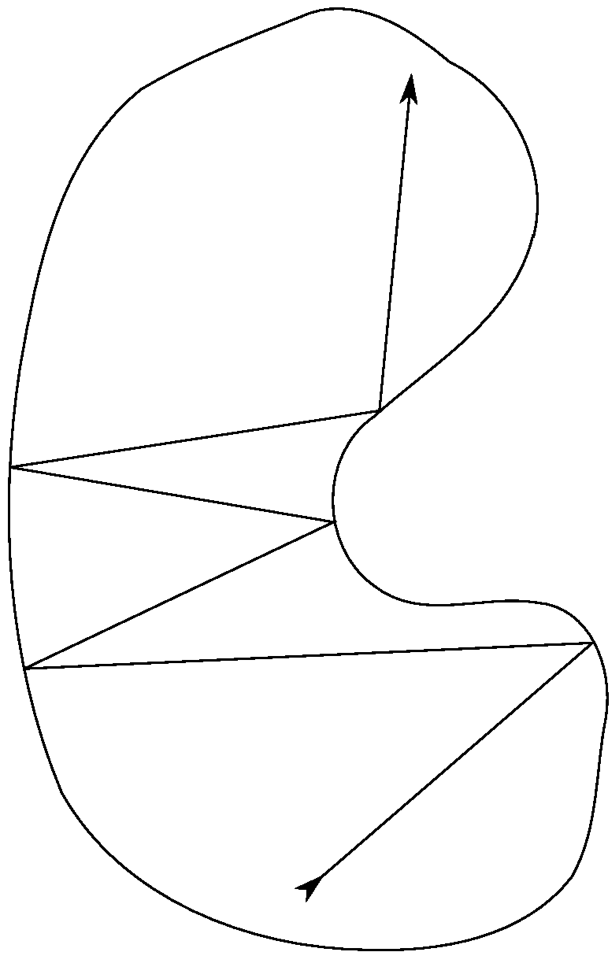

Figure 2: Example of optical ray with only transversal reflection points.

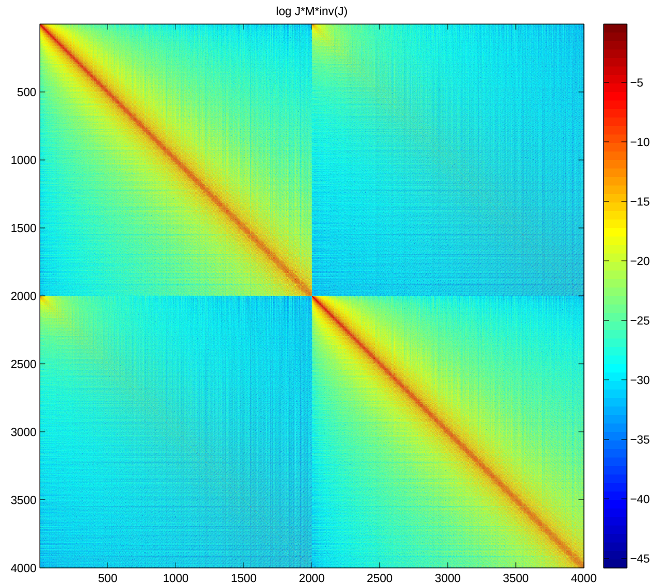

Figure 3: View of the logarithm of the coefficients of the matrix JM_TJ^{-1}, for the square geometry, with smooth control. This illustrates decay estimates (51) and (52).

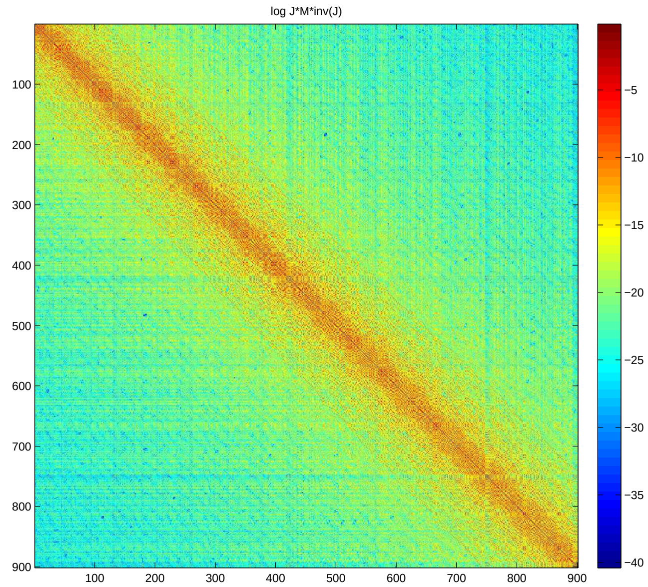

Figure 4: View of the logarithm of the coefficients of the matrix JM_TJ^{-1}, for the square geometry, with smooth control (zoom). This illustrates decay estimate (51).

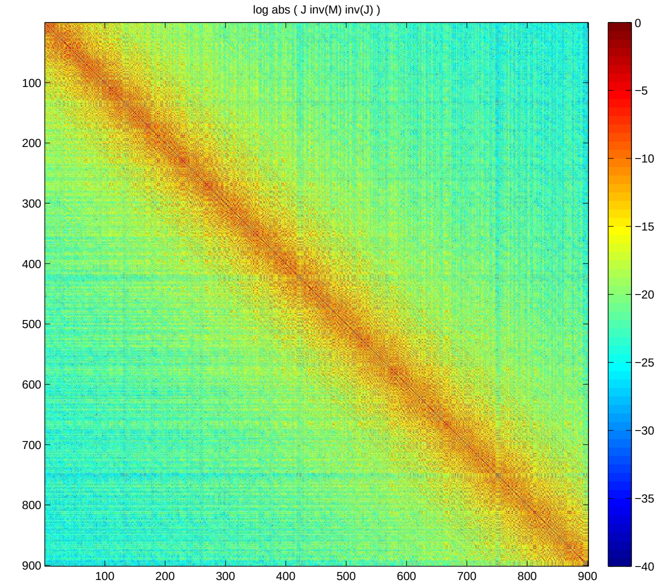

Figure 5: View of the logarithm of the coefficients of the matrix $JM_T^{-1}J^{-1}$, for the square geometry, with smooth control (zoom).

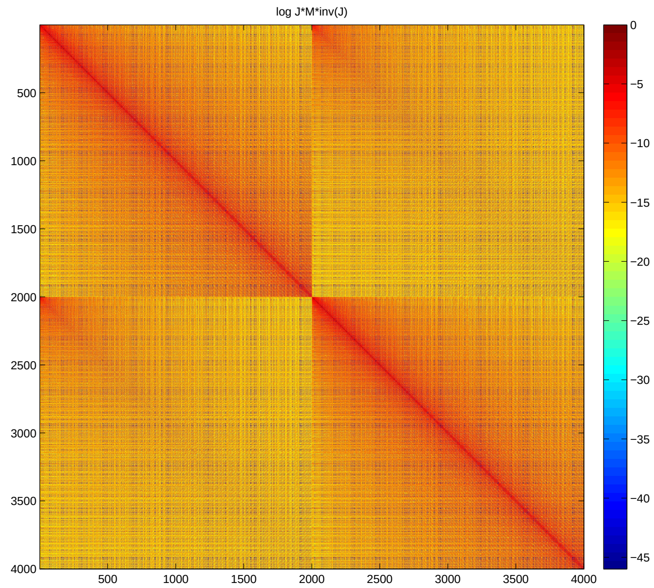

Figure 6: View of the logarithm of the coefficients of the matrix JM_TJ^{-1}, for the square geometry, with non-smooth control. Note that the color scaling is the same as in Figure 3.

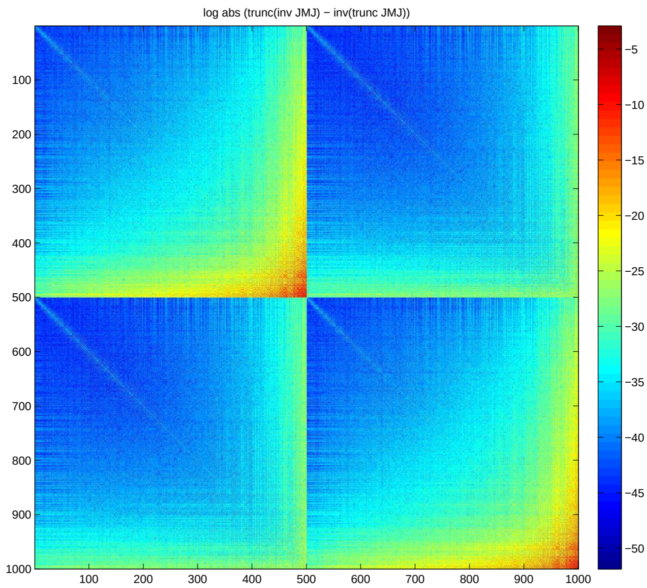

Figure 7: View of the logarithm of the coefficients of the matrix $J\left[((M_T)^{-1})_\omega - ((M_T)_\omega)^{-1}\right]J^{-1} = J\left[\Lambda_\omega - ((M_T)_\omega)^{-1}\right]J^{-1}$, for the square geometry, with smooth control. The M_T matrix is computed with 2000 eigenvalues, the cutoff frequency ω being associated with the 500th eigenvalue.

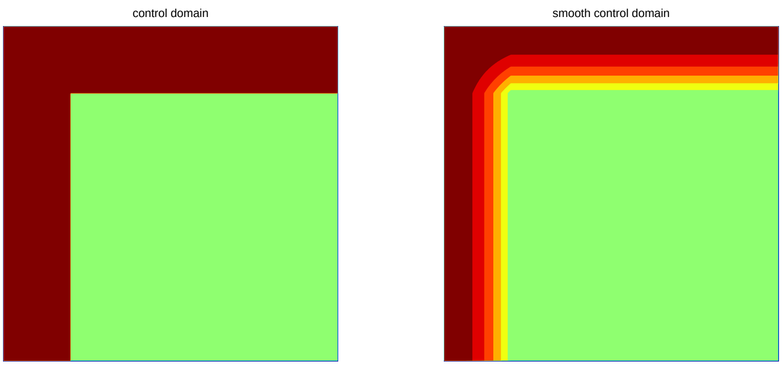

Figure 8: Domain and example of a control domain for the square, with smoothing in space (right panel) or without (left panel).

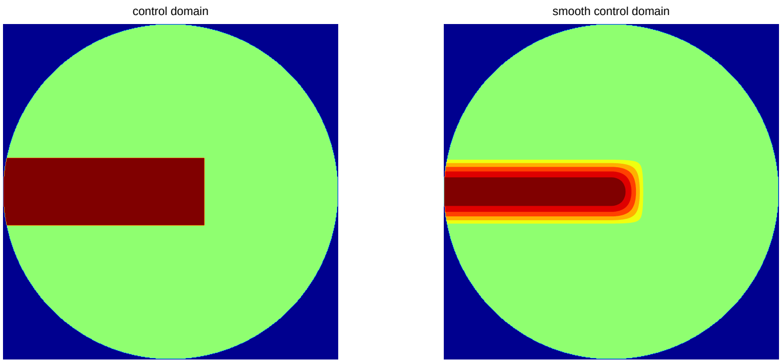

Figure 9: Domain and example of a control domain for the disc, with smoothing in space (right panel) or without (left panel).

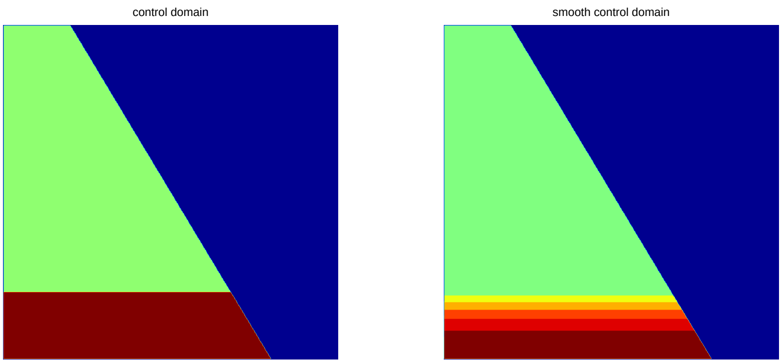

Figure 10: Domain and example of a control domain for the trapezoid, with smoothing in space (right panel) or without (left panel).

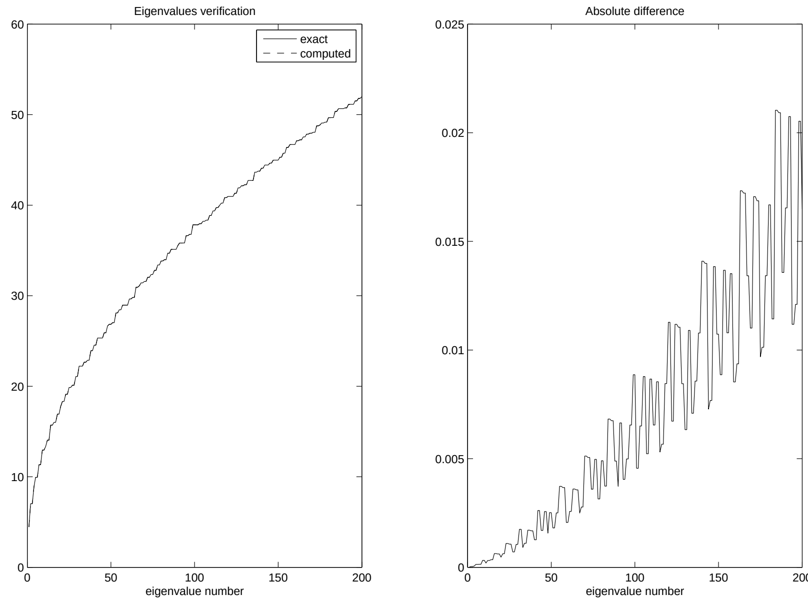

Figure 11: Verification of the eigenvalues computation in the square: exact and finite-differences-computed eigenvalues (left panel), and their absolute difference (right panel).

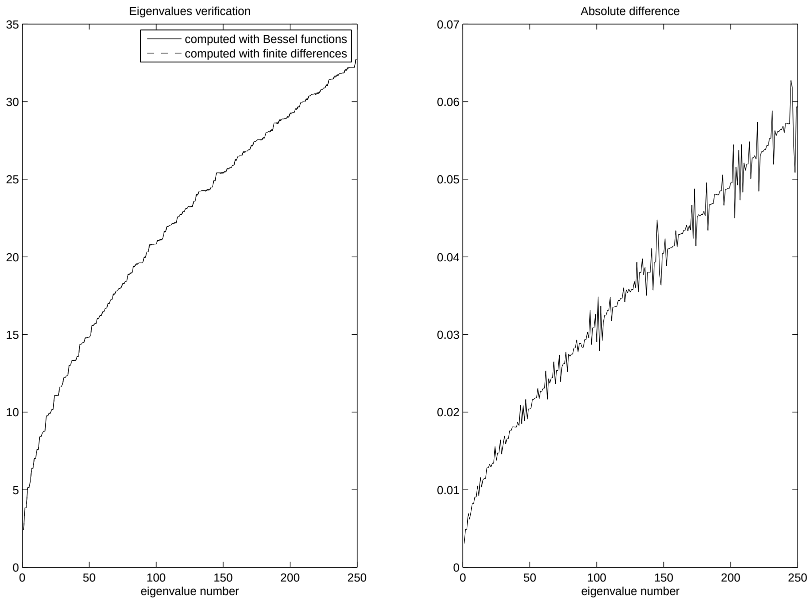

Figure 12: Verification of the eigenvalues computation in the disc: eigenvalues computed either as zeros of Bessel functions or with finite differences (left panel), and their absolute difference (right panel).

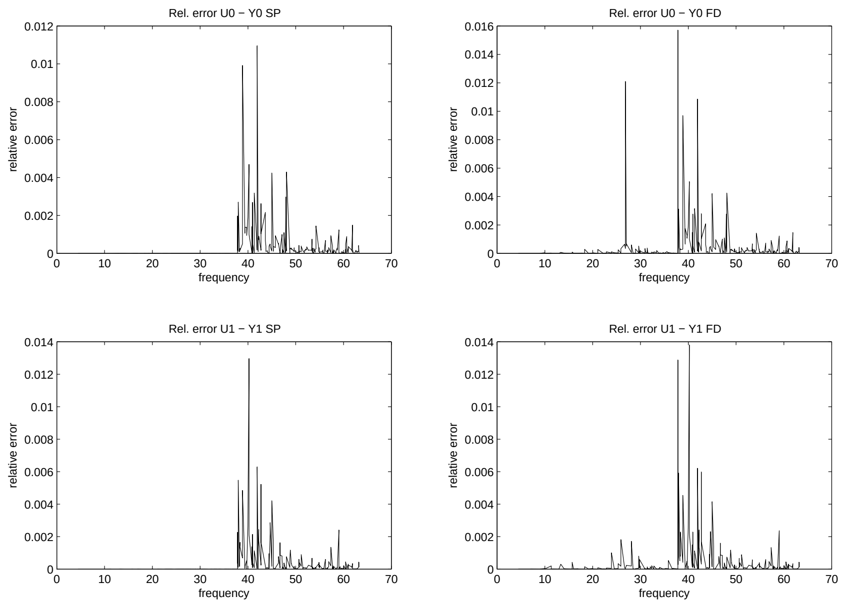

Figure 13: Validation experiments in the square: Relative errors between the spectral coefficients of the original function u and the reconstructed function y, computed with exact eigenvalues (left panels) or finite differences eigenvalues (right panels), for u_0 and y_0 (top panels) or u_1 and y_1 (bottom panels). The errors are plotted as a function of the frequency of the eigenvalues. The computation are performed with 100 eigenvalues, corresponding to a frequency of about 38, the reconstruction with 2000, corresponding to a frequency of about 160. For the readability of the figure, we plot only the major counterparts of the error, i.e. we stop the plot after frequency 63 (300th eigenvalue).

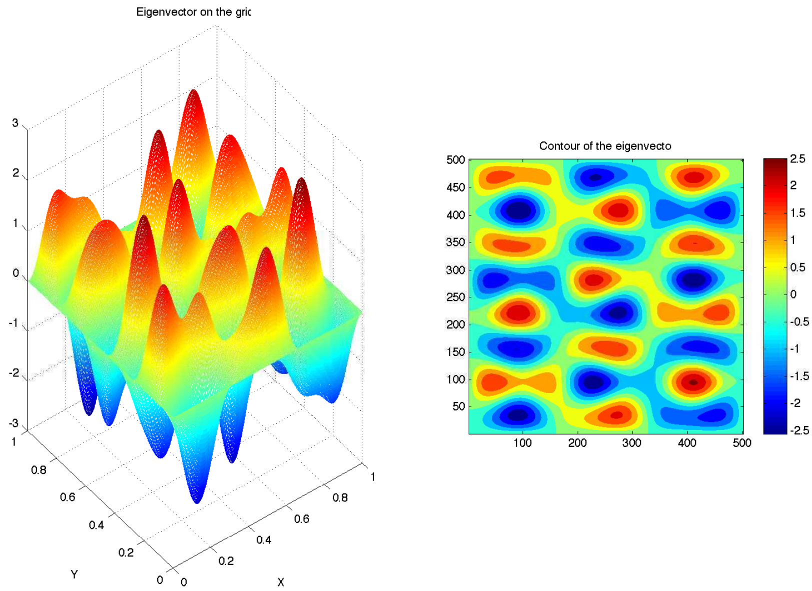

Figure 14: Representation on the grid in 3D (left panel) or contour plot (right panel) of the 50-th eigenvector in the square.

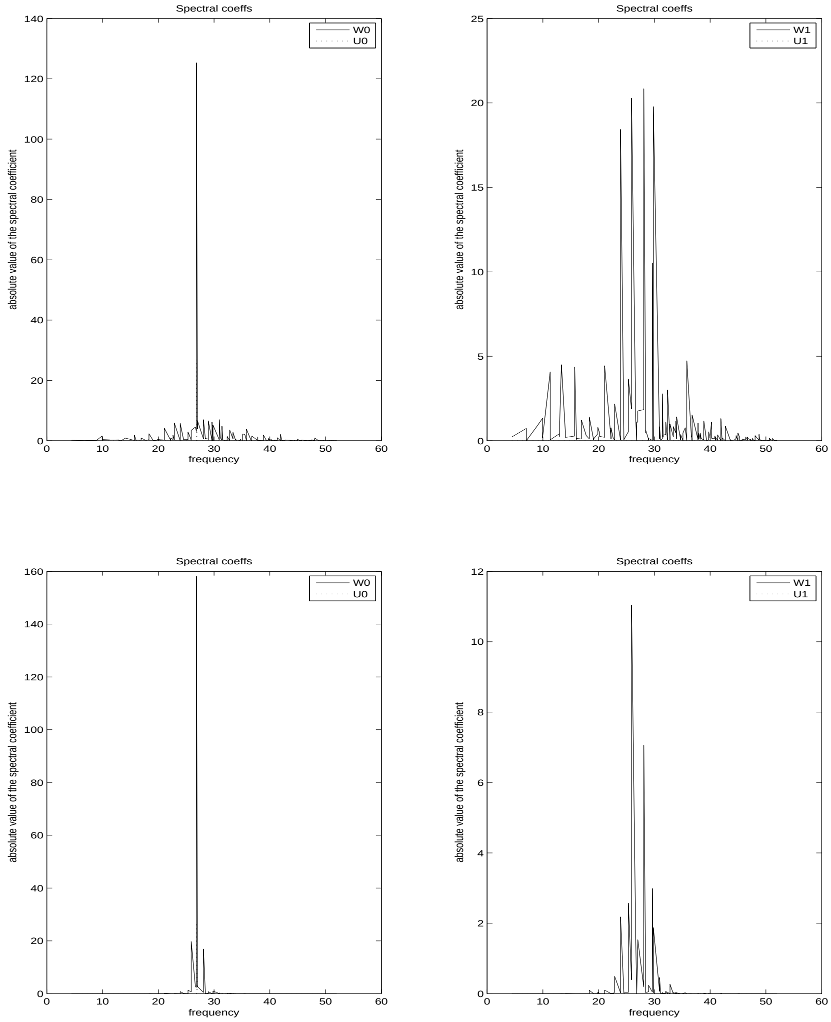

Figure 15: One-mode experiment in the square: localization of the Fourier frequences of (u_0, u_1) (dashed line) and (w_0, w_1) (solid line) for a given time T and a given domain U without smoothing (top) and with time- and space-smoothing (bottom). The x-coordinate represents the eigenvalues. The input data u_0 is equal to the 50-th eigenvector, equal to an eigenvalue of about 26.8, and $u_1 = 0$.

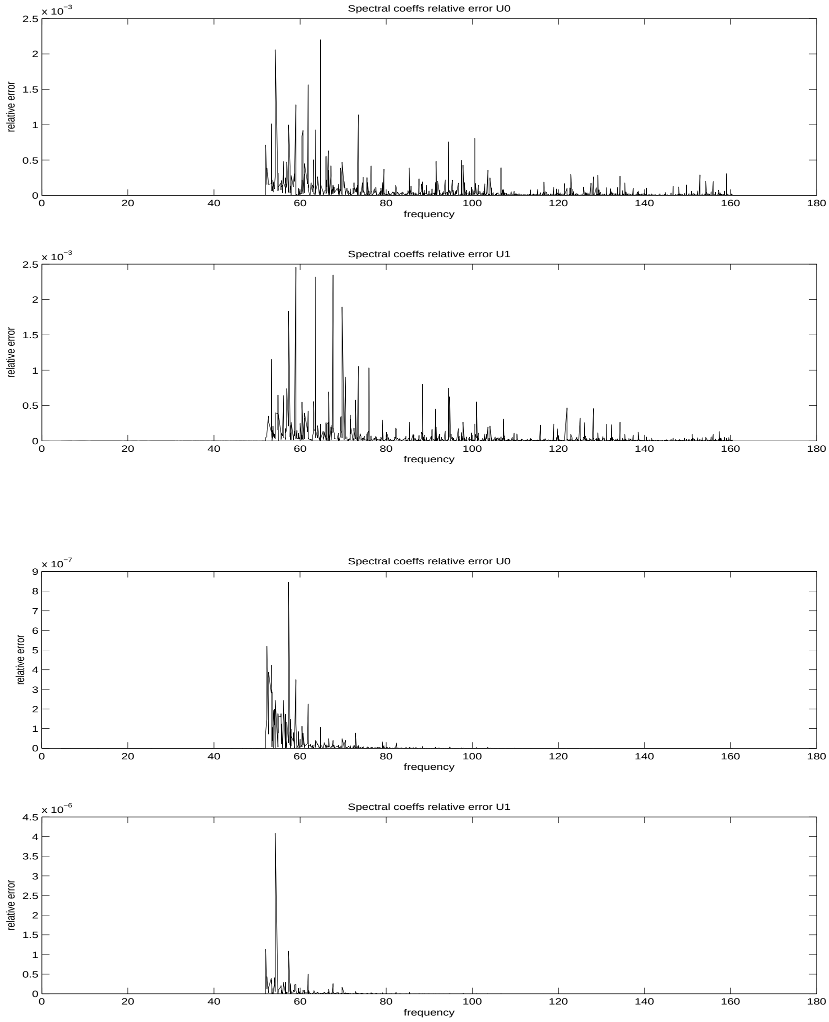

Figure 16: One-mode experiment in the square: localization of the Fourier coefficients of $(u_0 - y_0, u_1 - y_1)$, where u is the data and y is the reconstructed function obtained from the control function w, for a given time T and a given domain U without smoothing (top panels) and with time- and space-smoothing (bottom panels).

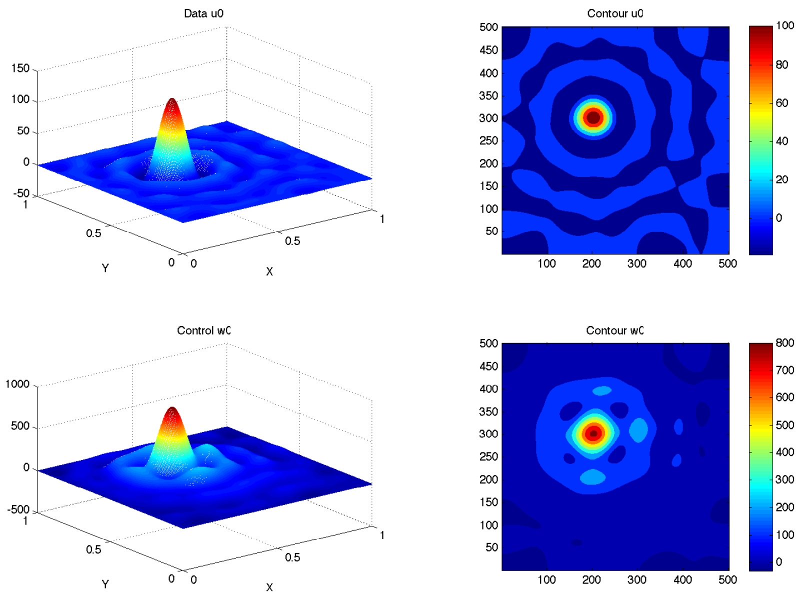

Figure 17: Space localization of the data u_0 (top panels) and the control w_0 (bottom panels), for a Dirac experiment in the square, with exact eigenvalues. These plots correspond to an experiment without smoothing, but it is similar with smoothing. Left panels represent 3D view, and right panels show contour plots.

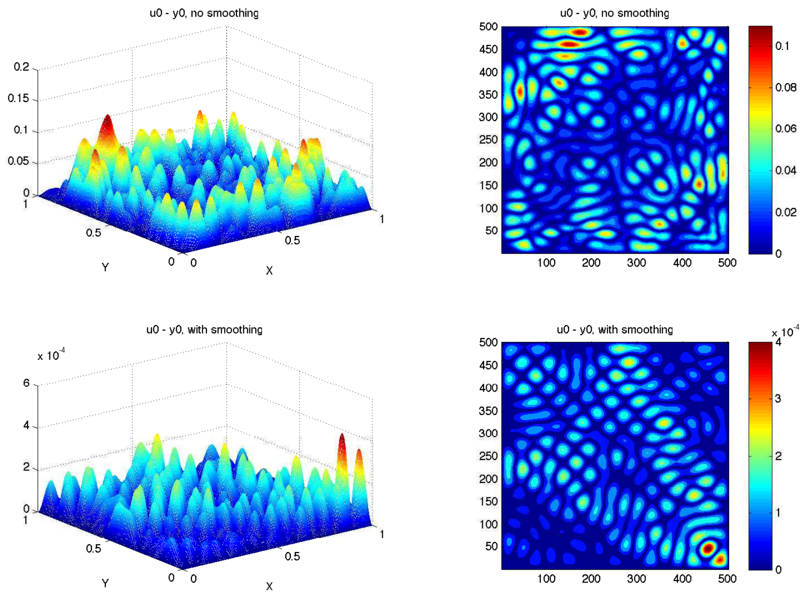

Figure 18: Difference between the data u_0 and the reconstructed function y_0 without smoothing (top panels) and with smoothing (bottom panels) for a dirac experiment in the square, with exact eigenvalues. Left panels represent 3D view, and right panels show contour plots.

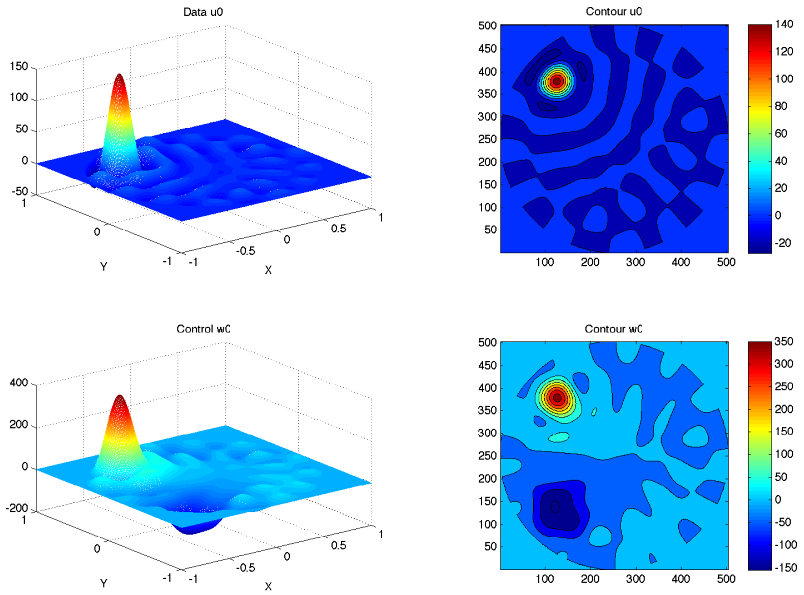

Figure 19: Space localization of the data u_0 (top panels) and the control w_0 (bottom panels), for a dirac experiment in the disc. These plots correspond to an experiment without smoothing, but it is similar with smoothing. Left panels represent 3D view, and right panels show contour plots. In this experiment, the input data is defined with $N_i = 100$ eigenvectors.

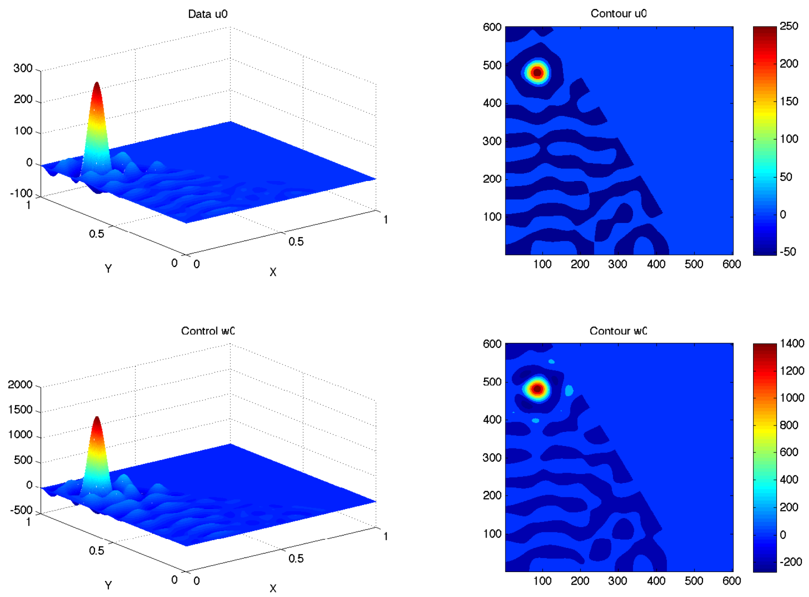

Figure 20: Space localization of the data u_0 (top panels) and the control w_0 (bottom panels), for a dirac experiment in the trapezoid. These plots correspond to an experiment without smoothing, but it is similar with smoothing. Left panels represent 3D view, and right panels show contour plots. In this experiment, the input data is defined with $N_i = 120$ eigenvectors.

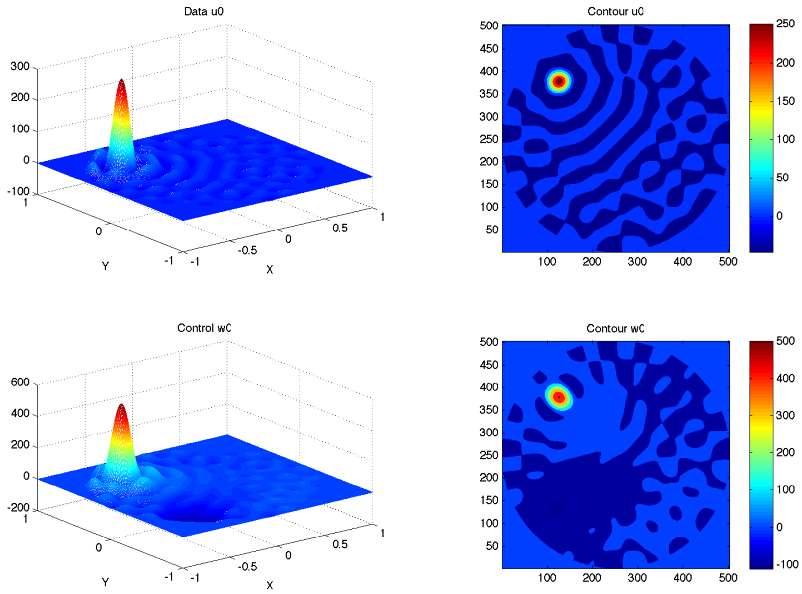

Figure 21: Space localization of the data u_0 (top panels) and the control w_0 (bottom panels), for a dirac experiment in the disc. These plots correspond to an experiment with smoothing, and it is similar without smoothing. Left panels represent 3D view, and right panels show contour plots. In this experiment, the input data is defined with $N_i = 200$ eigenvectors.

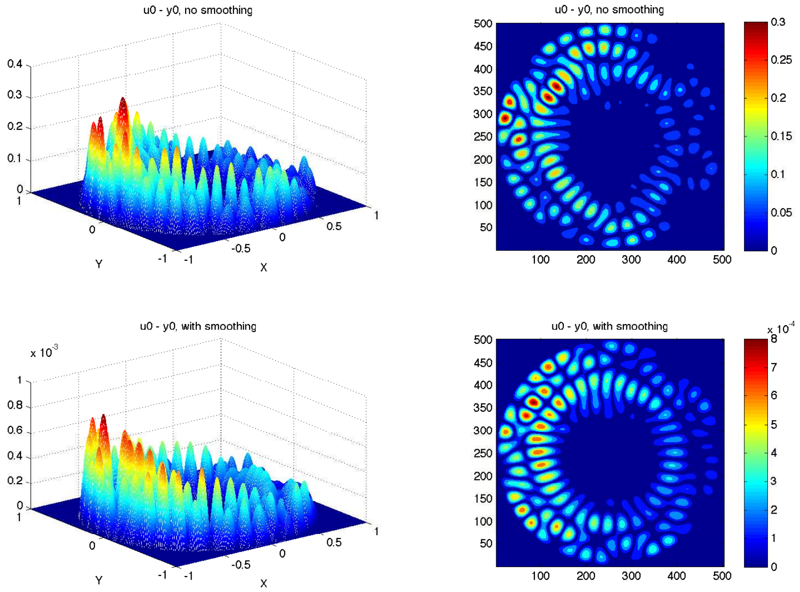

Figure 22: Difference between the data u_0 and the reconstructed function y_0 for a dirac experiment in the disc without smoothing (top panels) and with time- and space-smoothing (bottom panels). Left panels represent 3D view, and right panels show contour plots. In this experiment, the input data is defined with $N_i = 100$ eigenvectors.

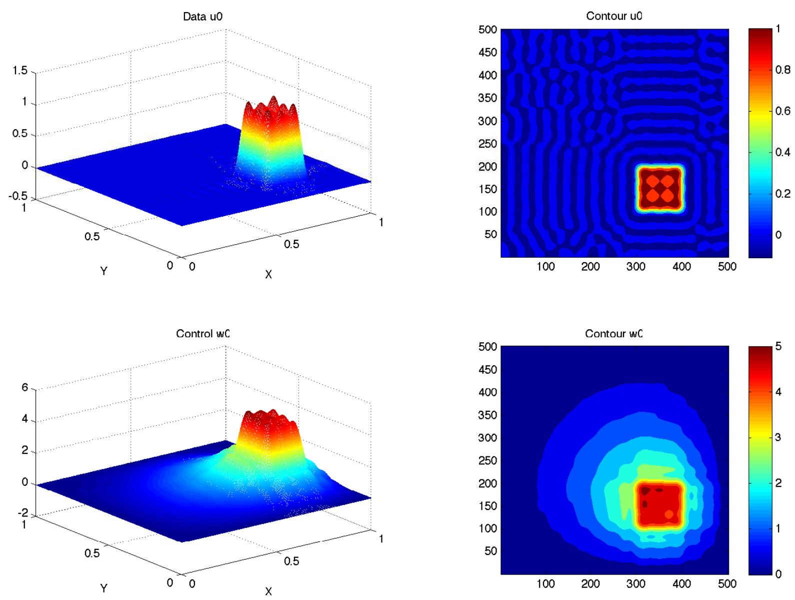

Figure 23: Space localization of the control function w_0 (bottom panels) with respect to the data u_0 (top panels), in the square, without smoothing: 3D plots on the left, and contour plots on the right.

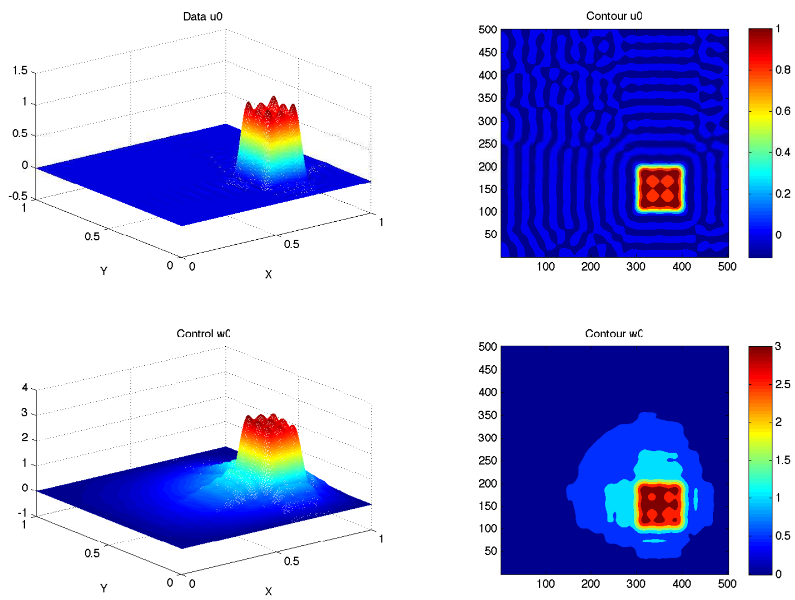

Figure 24: Space localization of the control function w_0 (bottom panels) with respect to the data u_0 (top panels), in the square, with smoothing. Left panels represent 3D view, and right panels show contour plots.

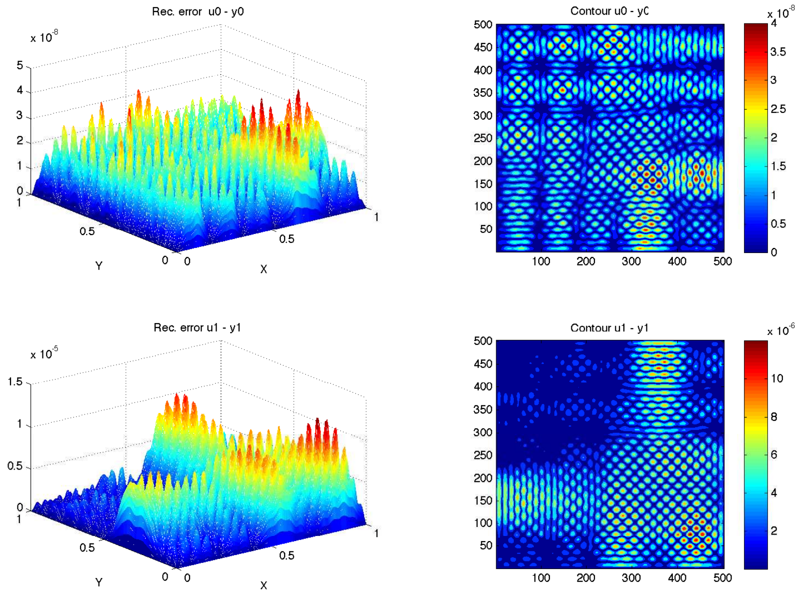

Figure 25: Difference between the data u_0 and the reconstructed function y_0 (top panels) and u_1 and y_1 (bottom panels) with smoothing in the square. The data is the identity function of a square whose edges are parallel to the x and y axes. Left panels represent 3D view, and right panels show contour plots.

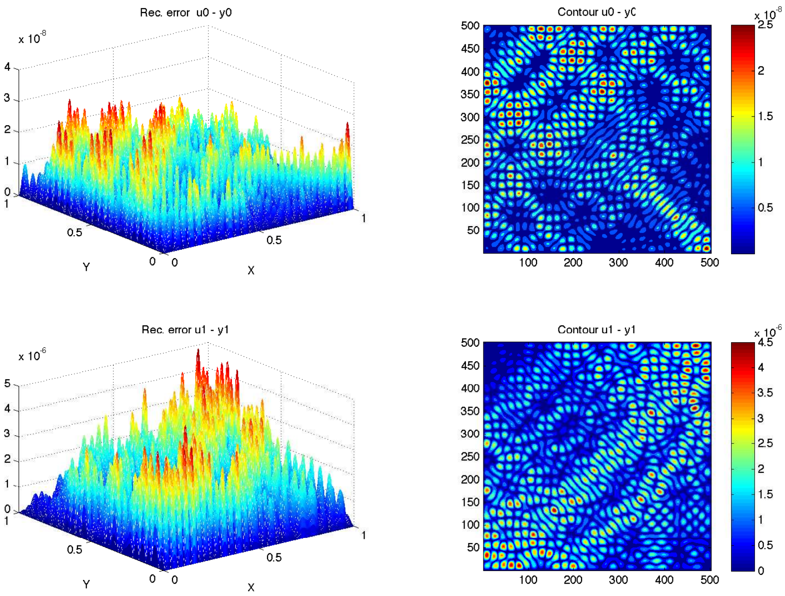

Figure 26: Difference between the data u_0 and the reconstructed function y_0 (top panels) and u_1 and y_1 (bottom panels) with smoothing in the square. The data is the identity function of a square whose edges are parallel to the diagonals of the square. Left panels represent 3D view, and right panels show contour plots.

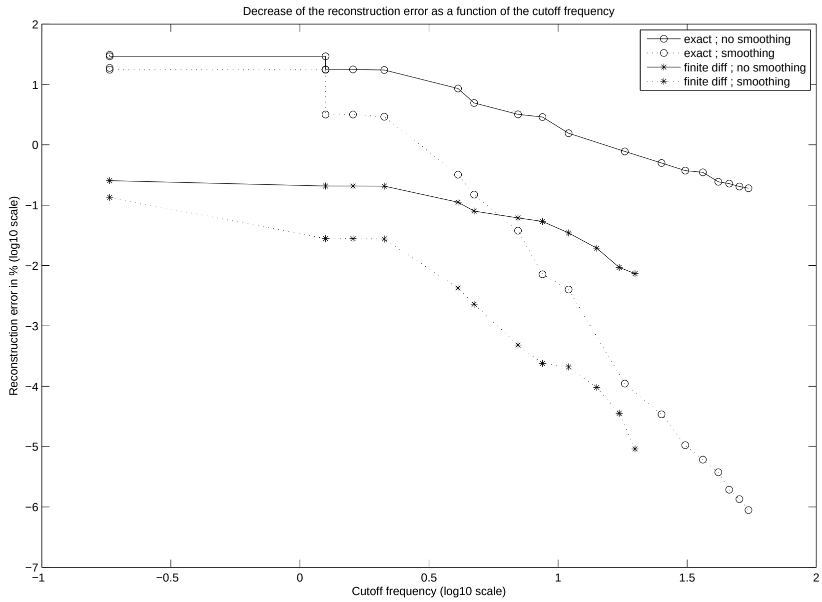

Figure 27: Reconstruction errors for the finite differences and exact methods, as a function of the cutoff frequency (i.e., the largest eigenvalue used for the control computation), with or without time- and space-smoothing.

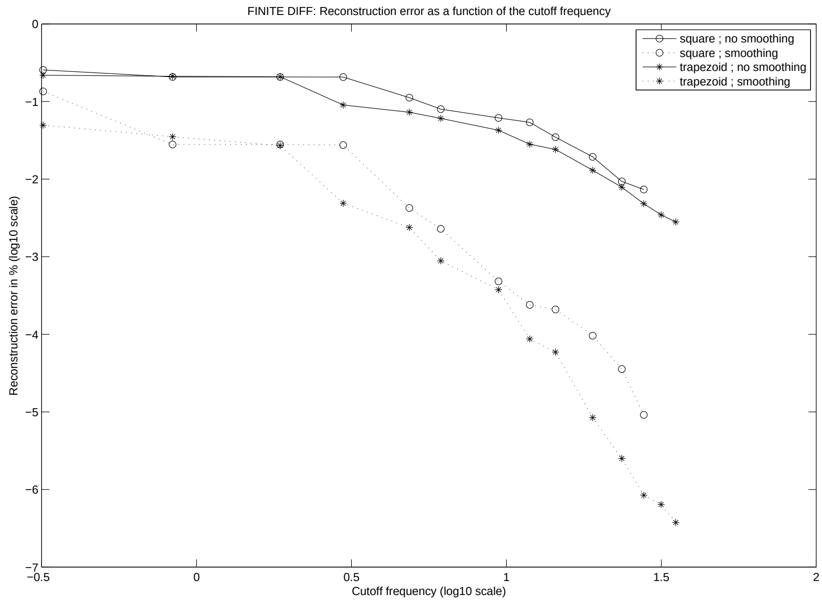

Figure 28: Reconstruction errors for the finite differences method, in the square and in the trapezoid, as a function of the cutoff frequency (i.e., the largest eigenvalue used for the control computation), with or without time- and space-smoothing.

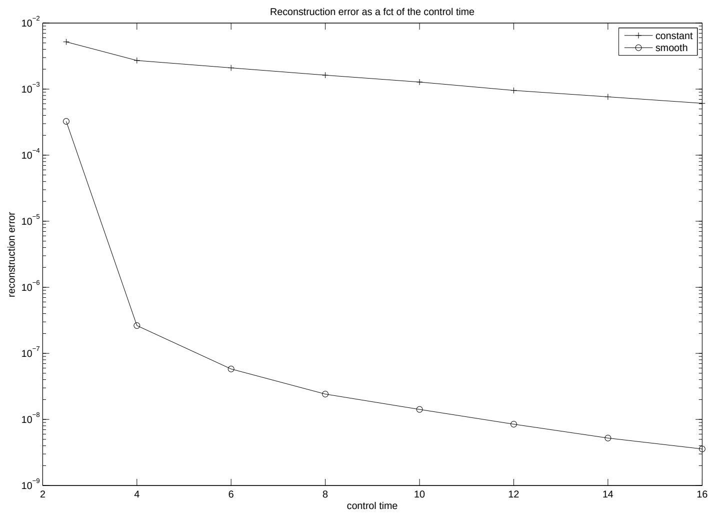

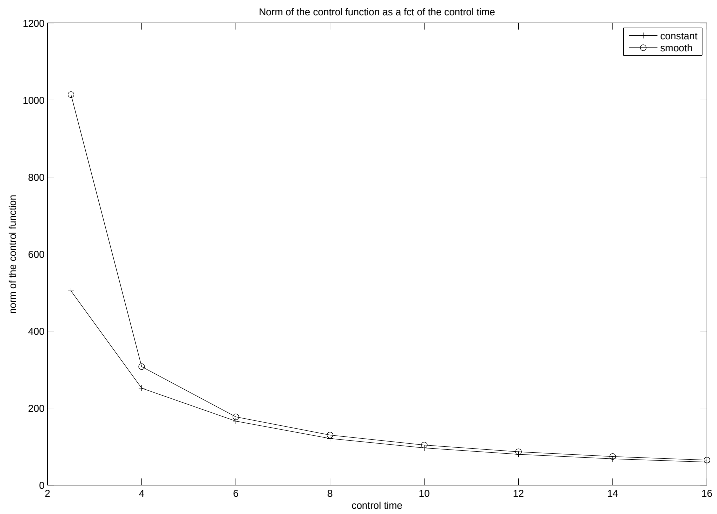

Figure 29: Experiments in the square, with exact eigenvalues: impact of the smoothing on the reconstruction error (top) and on the norm of the control function (bottom), as a function of the control time.

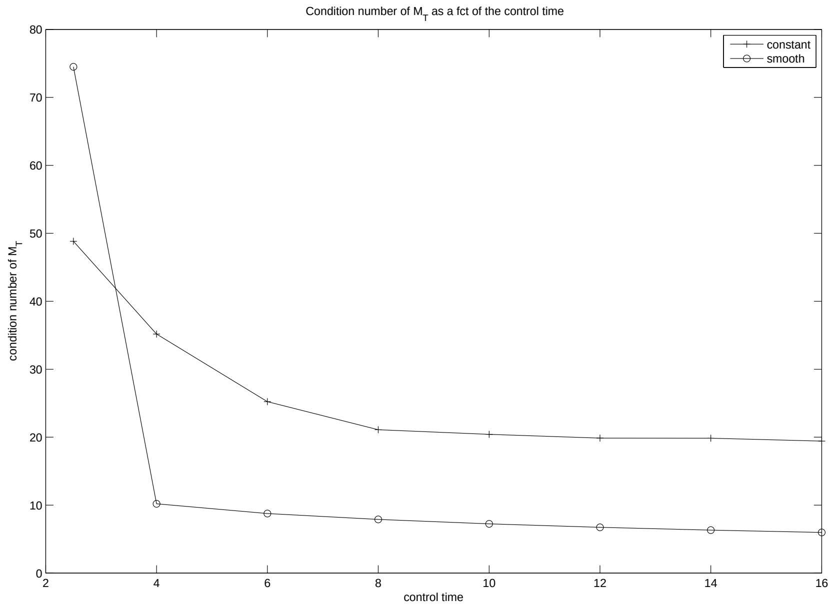

Figure 30: Experiments in the square, with exact eigenvalues: impact of the smoothing on the condition number of the M_T matrix, as a function of the control time.

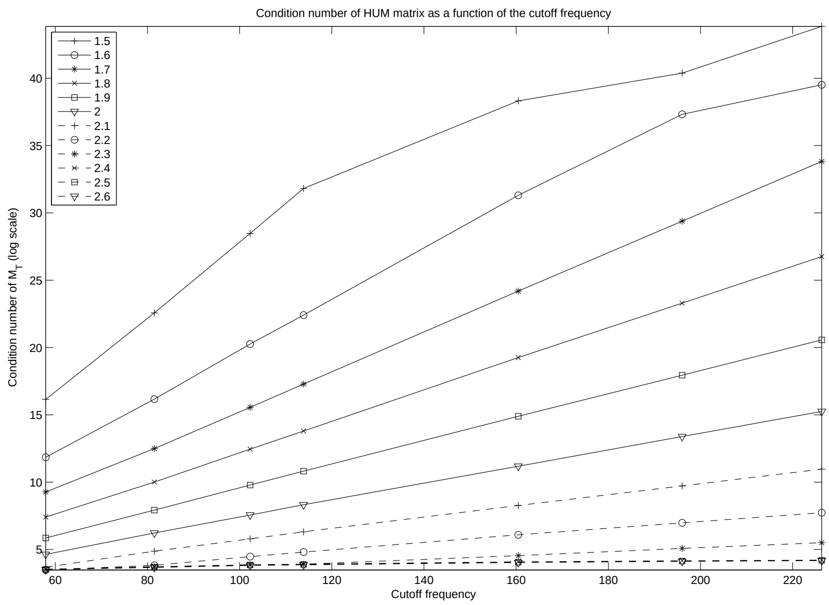

Figure 31: Condition number of the $M_{T,\omega}$ matrix as a function of the cutoff frequency ω for various control times.

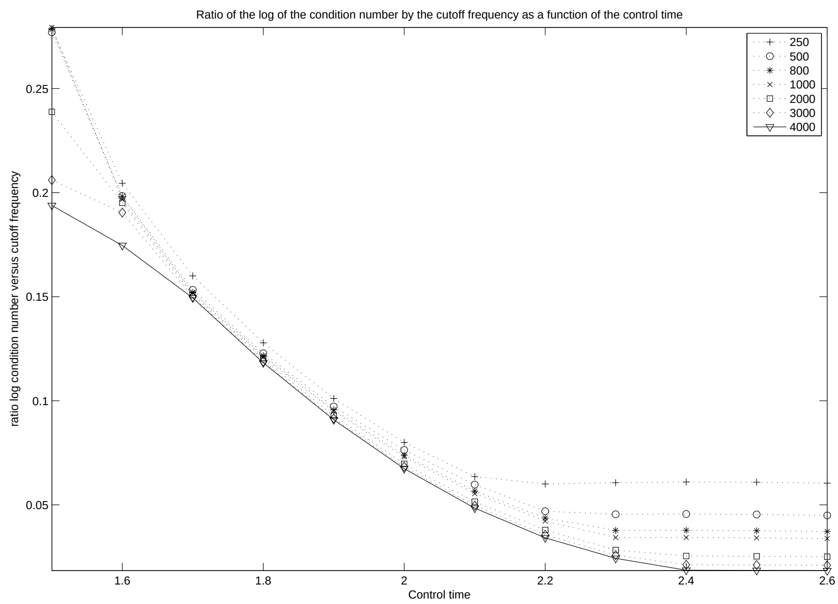

Figure 32: Ratio of the log of the condition number of the $M_{T,\omega}$ matrix and the cutoff frequency ω, as a function of the control time for various eigenvalues numbers.

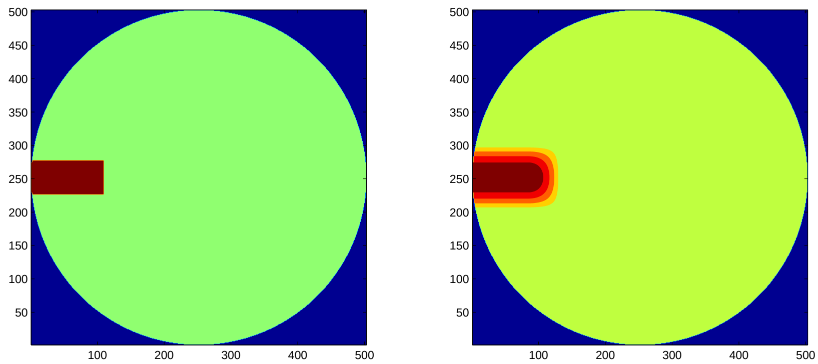

Figure 33: Non-controlling domain U without (left) or with (right) smoothing. This domain consists of the neighborhood of a radius which is truncated around the disc boundary.

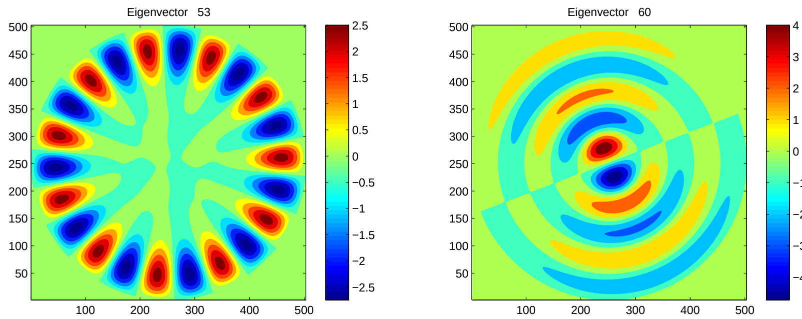

Figure 34: Special modes chosen for experiment with non-controlling domains, corresponding to the 53rd and 60th eigenvalues.

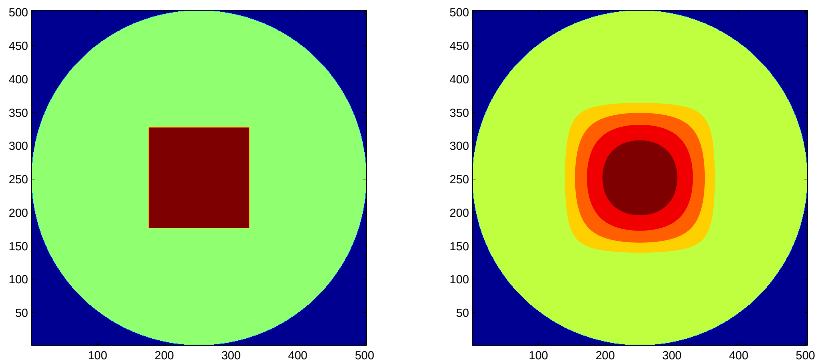

Figure 35: Non-controlling domain U without (left) or with (right) smoothing. This domain consists of the neighborhood of a radius which is truncated around the disc center.

List of Tables

Eigenvalues computation	Condition Number	Reconstruction error
Finite differences	7.4	1.8 %
Exact	7.5	1.6 %

Table 1: Validation experiments in the square: Condition numbers and validation errors for a 100-eigenvalues-experiment in the square (without smoothing), where the eigenvalues are exact or computed thanks to finite differences.

	Condition Number		Reconstruction error	
N_e	Exact	Finite differences	Exact	Finite differences
52	6.5	6.4	29.2%	29.0%
55	6.6	6.6	17.7%	17.6%
60	6.6	6.6	17.3%	17.2%
70	7.1	7.0	4.9 %	5.0 %
80	7.3	7.2	3.2 %	3.3 %
100	7.5	7.4	1.6 %	1.8 %
200	8.3	8.3	0.5 %	1.0 %
300	8.8		0.3 %	
500	9.5		0.2 %	

Table 2: Validation experiments in the square: Condition numbers and validation errors for various numbers N_e of eigenvalues used to compute the control function, where the eigenvalues are exact or computed thanks to finite differences. The input data is the 50-th eigenvalue, and the reconstruction is performed with 2000 eigenvalues.

Smooth	Width of U	Time	Condition number	Rec. error	$\|w\|$
no	1/10	2.5	48.8303	0.00518843	504.287
yes	2/10	2.5	204.048	0.00140275	1837.12
yes	2/10	4.7	21.7869	4.65892E-07	364.013
no	1/10	8	21.1003	0.00162583	120.744
yes	2/10	8	16.5497	8.51442E-08	189.361
yes	2/10	15	12.017	8.39923E-09	100.616
no	3/10	2.5	4.20741	0.0014823	147.009
yes	6/10	2.5	9.05136	1.94519E-06	336.704
yes	6/10	4.7	3.09927	2.99855E-08	125.481
no	3/10	8	3.20921	0.000488423	39.9988
yes	6/10	8	2.74172	6.0204E-09	69.8206
yes	6/10	15	2.4113	8.55119E-10	37.1463

Table 3: Impact of the control time, the width of U and the smoothing, on the condition number of M_T, on the reconstruction error and on the norm of the control function. These results come from one-mode experiments in the square, with exact eigenvalues.

smooth?	Condition number	53rd Eigenmode Rec. error	$\|w\|$	60th Eigenmode Rec. error	$\|w\|$
no	4960	0.63%	15	26%	4583
yes	6042	$6.5\ 10^{-4}$%	24	0.11%	8872

Table 4: Influence of the shape of the data on the reconstruction error and the norm of the control, with a non-controlling domain U. On the left, the 53rd eigenmode is localized around the boundary of the circle, as is the control domain. On the right, the 60th eigenmode is localized around the center of the circle.

	First domain			Second domain		
smooth?	Cond. nb.	Rec. error	$\|w\|$	Cond. nb.	Rec. error	$\|w\|$
no	4960	0.63%	15	$3.6\ 10^6$	68%	$1.9\ 10^4$
yes	6042	$6.5\ 10^{-4}$%	24	$3.3\ 10^5$	$9.4\ 10^{-3}$%	$6.5\ 10^5$

Table 5: Reconstruction error and the norm of the control with a data u_{53} localized at the boundary of the disc and two different non-controlling domains U, the first one being localized around the boundary, the second one around the center.